ABSTRACT

Title of Thesis:	FINITE ELEMENT MODELING AND CELLULAR STUDIES ON CONTROLLED PORES WITH SUB-SURFACE CONTINUITY FOR BIOMEDICAL APPLICATIONS
	Paul Keslar Lambert, Master of Science, 2012
Thesis Directed By:	Professor Sreeramamurthy Ankem Department of Materials Science and Engineering

This work investigated a novel process for improving the reliability of load-bearing joint prosthetics, in which electrical discharge machining (EDM) is used to create pores with sub-surface continuity on a conventionally-fabricated prosthetic material. The first part of this investigation utilized *in vitro* studies to verify the biocompatibility of deep, high-aspect-ratio EDM-produced pores. Mesenchymal stem cells were seeded onto Grade 4 titanium samples with EDM-created pores, and osteodifferentiation and mineralization were induced and assessed. It was found that such pores allowed for cell proliferation and mineralization indicating good biocompatibility. The second part of this work utilized three dimensional finite element modeling (FEM) to characterize simulated porous implant interfaces under stress. Interlocking strengths of selected structures were verified, interface separation under applied stress was measured for these structures with implications for wear particle intrusion in the interfaces, and stress shielding analysis was performed on simulated implants containing intersecting and non-intersecting pores.

FINITE ELEMENT MODELING AND CELLULAR STUDIES ON CONTROLLED

PORES WITH SUB-SURFACE CONTINUITY FOR BIOMEDICAL APPLICATIONS

By

Paul Keslar Lambert

Thesis submitted to the Faculty of the Graduate School of the
University of Maryland, College Park in partial fulfillment
of the requirements for the degree of
Master of Science
2012

Advisory Committee:
      Professor Sreeramamurthy Ankem, Chair
      Professor Mohamad Al-Sheikhly
      Professor John Fisher

Acknowledgements

I have many people to thank for their help and support while preparing this thesis. First and foremost are my family, who have always believed in my abilities and supported me wherever life has taken me. I am especially thankful to my Mom and Dad. They have taught me the importance of hard work and dedication, and the value of education. Thanks also to Michelle for all her love and support.

I would like to thank my adviser, Dr. Ankem, for directing my research and providing countless useful insights when the correct course of action was unclear. I am also grateful to Dr. John Fisher for his invaluable help in understanding bioengineering concepts during our frequent discussions. My sincere thanks go to Dr. Mohamad Al-Sheikhly as well, as he graciously contributed his time and effort reviewing this work as a member of my Thesis Committee alongside Dr. Ankem and Dr. Fisher.

I would also like to thank the entire faculty and staff of the Materials Science and Engineering Department, and the staff of the FabLab (especially Jon Hummel) for their assistance in completing this project. Thanks also to the other graduate students – notably Zane Wyatt, Will Joost, Kimberly Ferlin, Andrew Yeatts, and Emily Coates – who have been kind enough to lend me their assistance, instruction, insights, and support.

Table of Contents

List of Tables

List of Figures

Chapter 1

Introduction and Project Aims

Biomaterials are materials used to create artificial structures for replacing a lost or diseased biological structure and to restore form and function to the body [1]. Weight-bearing joints such as hip and knee joints are examples of structures in the body which commonly need to be replaced with biomaterial structures due to deterioration of the natural joint over the course of a patient's life. With improvements in joint replacement procedures and the increasing average human lifespan, the number of load-bearing joint replacement surgeries being performed has steadily increased in recent years, which in turn increases the need for reliability of these replacements [1-5].

From a materials standpoint, cementless weight-bearing joint implants must have high strength and toughness, and must also promote growth of healthy bone on and around the implant to maintain strong bone adhesion over time. In this regard, titanium and many of its alloys are popular in these applications for their high strength, low weight, corrosion resistance, wear resistance, and biocompatibility. However, one aspect of these prosthetic devices which stands to improve, regardless of the material used in constructing the device, is the operational lifetime. Many implantees require surgical revisions to their implants after only 10-15 years, because of implant loosening or excessive pain around the implant. In general, this loosening and/or pain can be attributed to three basic problems with current prosthetic joint technology: low interfacial connectivity and strength between the implant and the surrounding bone, poor stress transfer between implant and bone leading to bone resorption over time, and the intrusion

of wear particles from various implant components into the bone/implant interface and elsewhere in the effective joint space. The first two of these problems can lead to separation at the interface between bone and implant, causing eventual implant loosening; the third problem has been linked clinically to inflammation and pain in the area of the implant, although the link between bone/implant interface properties and wear particle intrusion is not fully understood.

Over the last several decades, much study has gone into altering the bone/implant interface to address the above-mentioned problems and increase the functional lifetimes of these implants. This body of work includes efforts to create implant materials which promote cell adhesion, maximize bone/implant contact area and increase mechanical interlocking through surface roughness, and improve implant/bone stress transfer via implant materials with lower elastic moduli [6-20].

In recent years, increased research emphasis has been put towards improving implant reliability by creating three-dimensional interconnectivity between bone and implant, such that separating the two requires bulk failure of one of the materials within the pore structure. This type of interconnectivity will herein be called "major mechanical interlocking." This major mechanical interlocking (contrasted with the conventional mechanical interlocking achieved by micro-roughness of the bone and implant surfaces) is desirable in prosthetics for several reasons. These include increased surface area for bone adhesion, reduced elastic modulus in the interlocked region (which will promote sustained adhesion over time), and the potential to sidestep weak bone/implant interface properties altogether by requiring bulk fracture of bone or titanium to cause utter failure at the interface.

This work continues the investigation of a newly-devised implant treatment process which is conducive to major mechanical interlocking with bone. This process was invented by S. Ankem (2008) and is currently being patented through the University of Maryland (U.S. patent application 12/754309). The process is used here with permission. It is predicted that this process – machining of pores with sub-surface continuity using electrical discharge machining (EDM) – may be as effective as other methods at promoting osseointegration of the implant while being simpler to perform and promoting better mechanical reliability of the implant once the process is optimized. The aims of this investigation are as follows:

1. Verify using *in vitro* cellular studies that a controlled structure of deep, high-aspect-ratio pores created using EDM will support osteoblast differentiation and mineralization. For EDM-produced major mechanical interlocking to be a viable implant treatment process, it must produce a biocompatible interface.

2. Perform FEM failure analysis on selected pore structures using FEM to determine approximate values for the interlocking strength of the bone/implant interface using the EDM method. The interlocking strength (which is a function of the mechanical properties of the bone and implant, the interfacial strength between them, and the geometry of their interconnectivity) is a measure of the implant's resistance to failure under static loading.

3. Assess the applied stress required to produce a fixed deformation at the apparent bone/implant interface for the interface structures created in Aim 2.

4. Qualitatively assess the effect of EDM-machinable pore interconnectivity on stress transfer from an FEM-simulated implant to the surrounding bone. This will give some indication of the stress shielding effect seen in an implant with this surface treatment compared with other implants.

A thorough literature review and technical background is provided in Chapter 2. Chapter 3 outlines the previous work on the EDM process leading up to this investigation. The results and discussion of the *in vitro* cell proliferation studies are provided in Chapter 4. Chapter 5 is a comprehensive review of the FEM mechanical property characterization done in this work, including results and discussion of the simulated failure analysis, interface deformation, and stress shielding behavior of selected pore structures. Lastly, Chapter 6 summarizes this investigation's main conclusions and Chapter 7 provides some potential avenues for future work.

Chapter 2

Technical Background

This chapter consists of a brief review of prosthetic implants, their constituent materials, the issues relating to the bone/implant interface in current implant technology, and the previous work addressing these issues.

2.1 Implant Technology

Weight-bearing joint replacement implants, in general, consist of three basic components: two components which anchor into the existing bone on either side of the joint, and a component which articulates the two anchors and allows a range of motion in the joint. Focusing specifically on a hip implant device, these components are called the acetabular component (a bowl-shaped piece which anchors into the acetabulum, a concave portion of the pelvis bone), the femoral stem component (a rod-shaped piece which is inserted into and anchors to the femur), and the femoral head (a sphere, connected at an angle to the femoral stem, which fits neatly within the acetabular component and allows motion of the stem relative to the acetabular component). The acetabular component will often also contain an insert which lowers the friction acting on the femoral head. These components are illustrated in Figure 2.1.
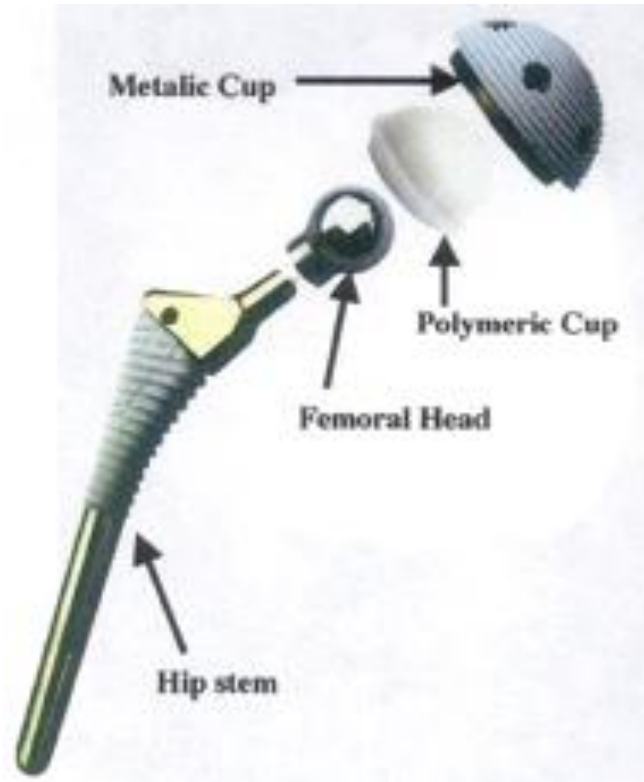
Figure 2.1: Schematic diagram showing the component parts of an artificial hip joint [5].

2.2 Implant Materials

Components of these prosthetics have been made from a wide variety of materials, including polymers (such as ultra-high molecular weight polyethylene), ceramics (such as alumina), metals (such as stainless steels, cobalt-chromium alloys, and titanium alloys) and composites (such as carbon fiber-reinforced polymer matrix composites) [21]. However, the strength and toughness requirements of load-bearing implants mean that metal is the preferred material class for the anchoring components of the implant. Among metals, titanium alloys are often the preferred material because of their high strength, low weight, low elastic modulus, corrosion resistance, wear resistance, and biocompatibility [1]. Especially in recent years, titanium alloys are

gaining popularity as a joint replacement material, despite their relatively high cost, due to the advantages they offer over other metals [1, 2].

2.3 Reliability of the Bone/Implant Interface

Regardless of implant material used, load-bearing joint prosthetics could stand to improve from a reliability standpoint. A small but significant number of implants fail after approximately 10-15 years, requiring surgery to revise the implant. (In this context, "failure" refers to either mechanical loosening of the implant, or pain in the implant sufficiently high that surgery is needed). Long-term failure of the implant can be attributed to three main causes: low bonding strength between the implant and bone, a bond which deteriorates over time due to stress shielding, and particle accumulation due to corrosion and wear. The causes, mechanisms and results of these failure types are summarized broadly in Figure 2.2.
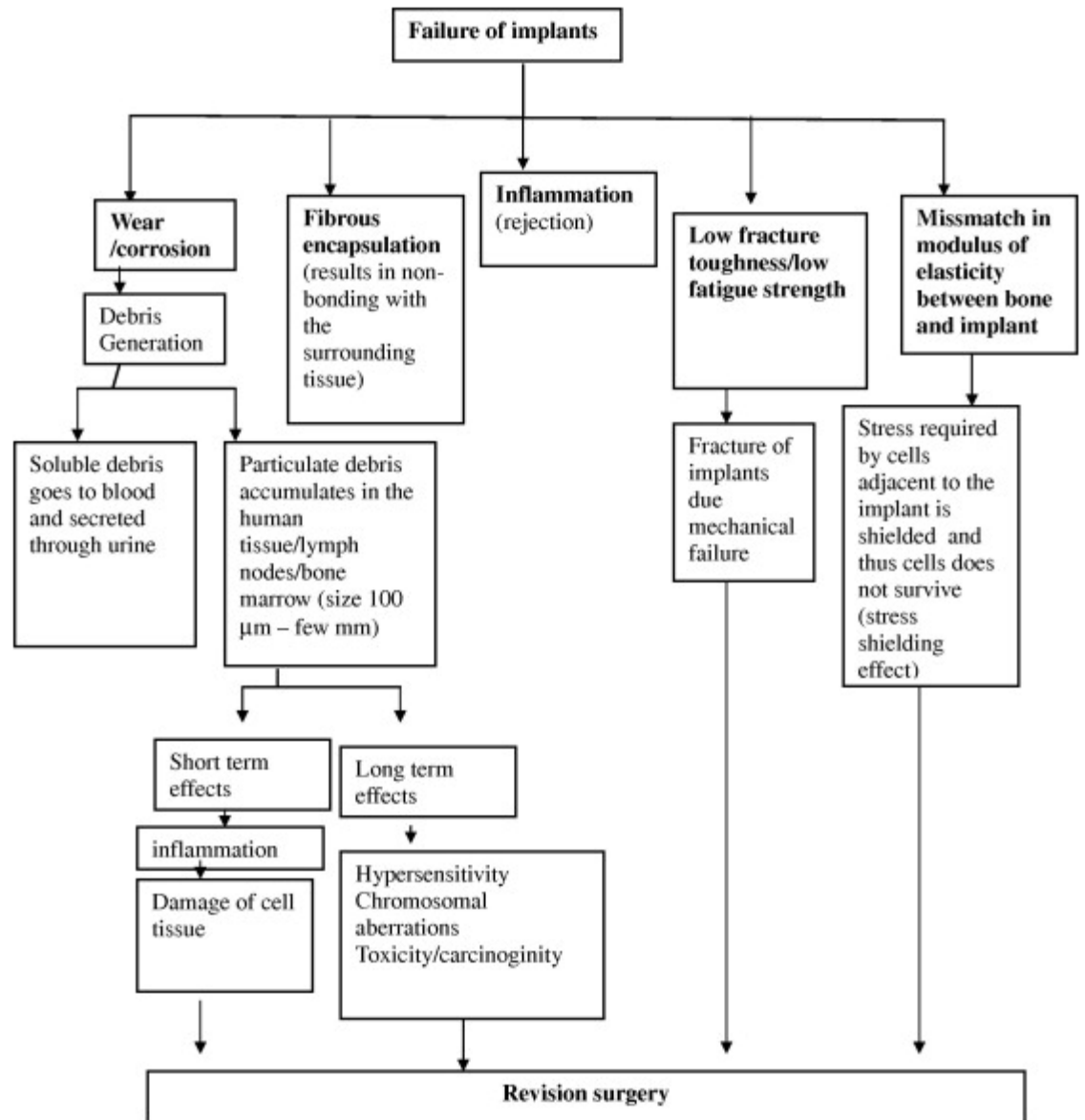
Figure 2.2: Summary of the causes of failure in prosthetic implants [1].

As stated above, one of the three root causes of this low implant longevity is the poor implant/bone interfacial strength achieved in the body. The candidate implant material must have a surface that is amenable to bone cell adhesion and which leads to strong chemical and physical bonds at the bone/implant interface. Currently, this

adhesion strength is significantly lower than both the strength of the implant material used and of bone itself. For example, metallic implant materials have yield strengths in the hundreds of megapascals, and bone will inelastically deform in the range of 45-150MPa, depending on the type of bone and the loading conditions. In contrast, the shear strengths of the bone/implant interfaces reported in the literature fall well below these values, and the tensile strength of the interface is almost zero. There is considerable variation in the interfacial shear strength attainable depending on the testing conditions and implant processing, but most fall within the range of 1.5-8MPa [22-24]. These values do not greatly exceed the peak stresses seen in the human hip joint during normal activity [25]. Although the stresses acting at the bone/implant interface are predominantly shear, there can also be tensile stresses acting under bending loads, and the strength of the interface under direct tensile loading is much less than 1MPa [26]. This very low tensile strength reflects the small amount of chemical bonding which occurs between bone and typical metals; the vast majority of connectivity comes from physical bonding via micro-roughness.

The second root cause of low implant longevity is the modulus mismatch between the implant material (~100GPa) and cortical bone (<20GPa) [27, 28]. When a composite is made of two materials with a large mismatch in elastic modulus, the material with the smaller modulus will experience stress shielding [27]. In the case of biomedical implants, the bone is shielded from stress by the implant, and the decreased stimulation to the bone is interpreted by the body as a decreased need for bone production in this area. Over time, this causes bone resorption and consequent implant loosening [1, 7, 27, 29]. In this regard, chemically pure titanium has a very low modulus as compared to the other

implant alloys and even lower modulus Ti alloys have been developed with non-toxic alloying elements [2, 30-34]; however, titanium's modulus is still much higher than bone's.

The third root cause of low implant longevity, and one frequently observed from a clinical standpoint, is pain often attributed to implant wear and corrosion particles in the effective joint space [35]. The fluids in the human body will corrode most metals over time, and repeated daily activity can produce many thousands of cycled loads on an implant, making them prone to wear. Both these mechanisms lead to the erosion of particulate material from the implant. Small, soluble debris may eventually exit the body, whereas larger particles (~100μm and above) tend to accumulate [1]. Clinical reports have identified polymer, metal, and ceramic implant material particles accumulating in implantees, although recent moves toward more wear-resistant materials in the femoral head and acetabular liner have produced improvements in this situation. Regarding particle intrusion near the bone/implant interface, the roles that interface properties play in intrusion rate and odds of implant failure are currently unclear. Small (sub-micron-sized) particles have been observed clinically near the interface of even well-fixed implants, so the ultimate solution to wear particle problems in the effective joint space might only be found in further improvements to implant wear resistance. However, poor bone/implant interfacial bonding provides a clear mechanism for accelerated particle intrusion, and some works indicate that the presence of wear particles is only incidental to pain and inflammation near the implant instead of a root cause of it [36], so improved bone/implant interface bonding over the life of the implant may mitigate problems attributed to wear particles as well.

2.4 Existing Implant Surface Treatments

A number of modifications to the bare metallic surface of a prosthetic implant have been used clinically or tested in an effort to remedy the problems mentioned in the above section. Some of the simplest methods used historically are mechanical modifications such as machining, grinding, or blasting the surface of the implant with hard particles in order to create a rough surface [5, 37]. These methods are the most cost effective, but often times are the least desirable in terms of cell adhesion. Chemical methods can also be used, including forced oxidation of the titanium surface or otherwise modifying the titanium's surface chemistry using techniques such as sol-gel or chemical vapor deposition [15, 38, 39]. In most cases, this results in a good cell adhesion but may contaminate the titanium's chemistry leading to the possibility of toxicity. An intermediary layer between the titanium and the bone in-growth such as bioactive hydroxyapatite or a lower-modulus surface layer may be applied using physical methods such as plasma spraying [40-46]. These methods can lead to improved bone adhesion, although the adhesion of the intermediary layer to the implant itself can prove problematic; this interface may not be dramatically stronger than the bone/titanium interface and is more prone to fatigue.

In addition to these methods of coating or roughening the metal surface, much work has been done on creating porous implant surfaces (especially those which allow for major mechanical interlocking). Porous implants have the two-fold benefit of increasing the surface area for bone to adhere to and reducing the effective elastic modulus around the bone/implant interface (due to the combination of voids and lower-modulus bone filling the pores). Porous implants have traditionally been accomplished

through the use of closed- or open-cell metal foams, or sintered powders, which create a randomly-arranged porosity on the implant [7, 47-52]. Bone ingrowth in these pore structures can noticeably improve implant adhesion, although foams and particles applied to the surface of a bulk implant create another interface (and possible failure site), and mechanical interlocking may be sub-optimal due to the random porosity. This applies for both the arrangement of the porosity as well as specific pore diameters and depths, as these variables impact the quality of bone ingrowth [53-57].

In recent years, increased research has gone into methods of creating implant surface porosity with a higher degree of control (where *control* refers to precise control over individual pore size, position, orientation, microstructure, and wall morphology) in order to maximize the benefits of bone ingrowth and interlocking. Additive techniques for creating continuous porosity with controlled architecture have been developed, generally based on the concept of 3-D printing (i.e. the implant is made incrementally by adding successive layers of metal powder). Common names for these techniques include rapid prototyping, electron beam melting, selective laser melting, and freeform fabrication [8, 9, 29, 58, 59]. Perhaps the most prevalent of these methods in the literature is electron beam melting (EBM). In this technique, a porous implant is modeled using computer-aided design (CAD). Then, a computer program partitions the model into layers ~0.05-0.2mm thick and this information is transferred to the manufacturing equipment. This equipment consists of an electron beam which scans across a bed of metal powder, selectively melting powder in regions which are to be part of the finished implant. Once all the portions of the implant from one layer of the computer drawing are melted and solidified, the powder bed is moved down by the

thickness of one model layer, and additional metal powder is spread across the top of the bed. The electron beam then melts the powder in positions corresponding to the second computer model layer, and this process repeats until the whole implant is created. This process must be performed under high vacuum, as the introduction of oxygen into the implant layers while they are molten or hot would cause extreme embrittlement of the implant. Some examples of porous implants that can be produced using EBM are shown in Figure 2.3, although in principle the types of porous structures which can be produced using this method are extremely varied.
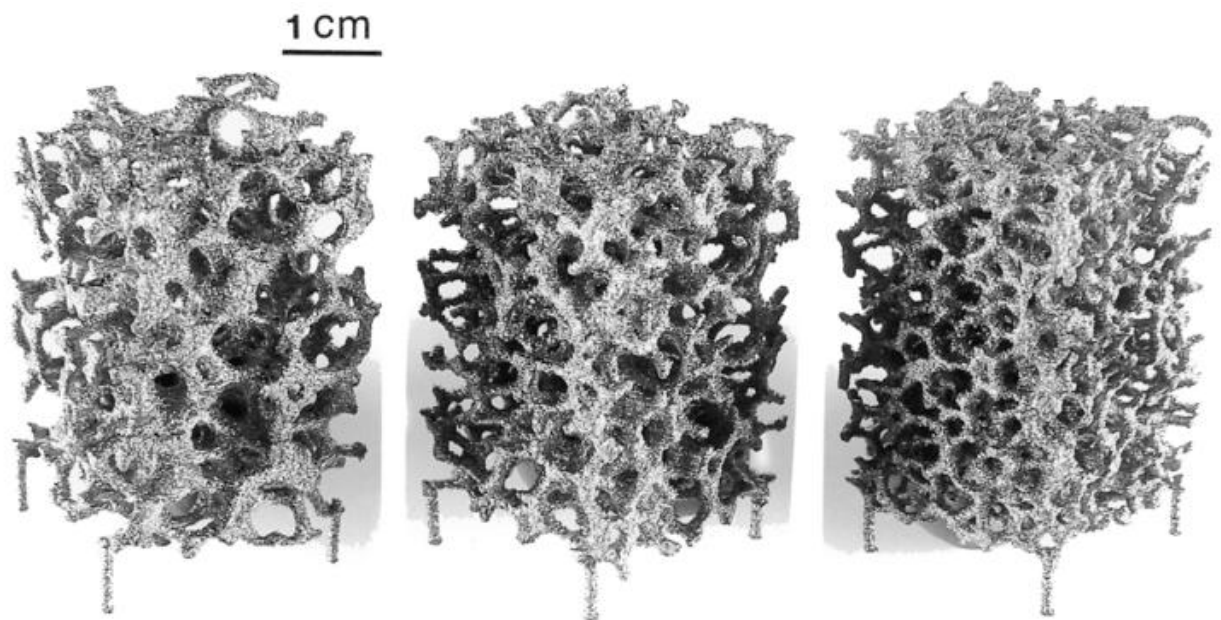
Figure 2.3: Examples of implant structures fabricated using electron beam melting (EBM) [19].

EBM and other rapid prototyping techniques show good results in terms of bone ingrowth and reduced elastic modulus near the interface, but possess drawbacks as well. The first is the jagged, notched pore wall morphology which stems from the layer-by-layer melting of the material during production. This causes the edges of each layer to

13

have an uncontrolled rounded shape based on the shape the metal powder assumes in the liquid state. Stacked together in many layers, this lead to a rough pore wall surface, an example of which is seen in Figure 2.4. Such a surface can lead to stress concentrations which, under tensile or bending loads, promote a lower failure strength and shortened fatigue life for the implant. Although few publications exist which describe the tensile and fatigue properties resulting from this relatively new process, many surface preparations such as laser processing reduce the failure strength and fatigue life of implant materials [60], and it is very likely that additive processes such as those mentioned above reduce these properties as well. Another disadvantage of these additive techniques is that the entire implant, including the porosity in its designed geometry, are created in the material as it solidifies. This means that modification of the implant microstructure through thermomechanical processes such as cold working cannot be done because they would alter the porosity from its intended shape (and cold working the porosity *into* some desirable geometry does not seem at all feasible). This means that certain materials which derive their desirable properties as an implant from extensive plastic deformation, such as low-modulus Ti-Nb-Ta-Zr alloys, cannot be used along with these processes. One additional shortcoming of EBM in particular is the machinery involved in the manufacturing process, which is relatively expensive and uncommon (in the current joint implant industry). This includes an electron beam apparatus and a high vacuum system, the latter of which particularly hinders the scale-up potential of this process. Most other rapid prototyping processes require similarly expensive and inconvenient equipment.
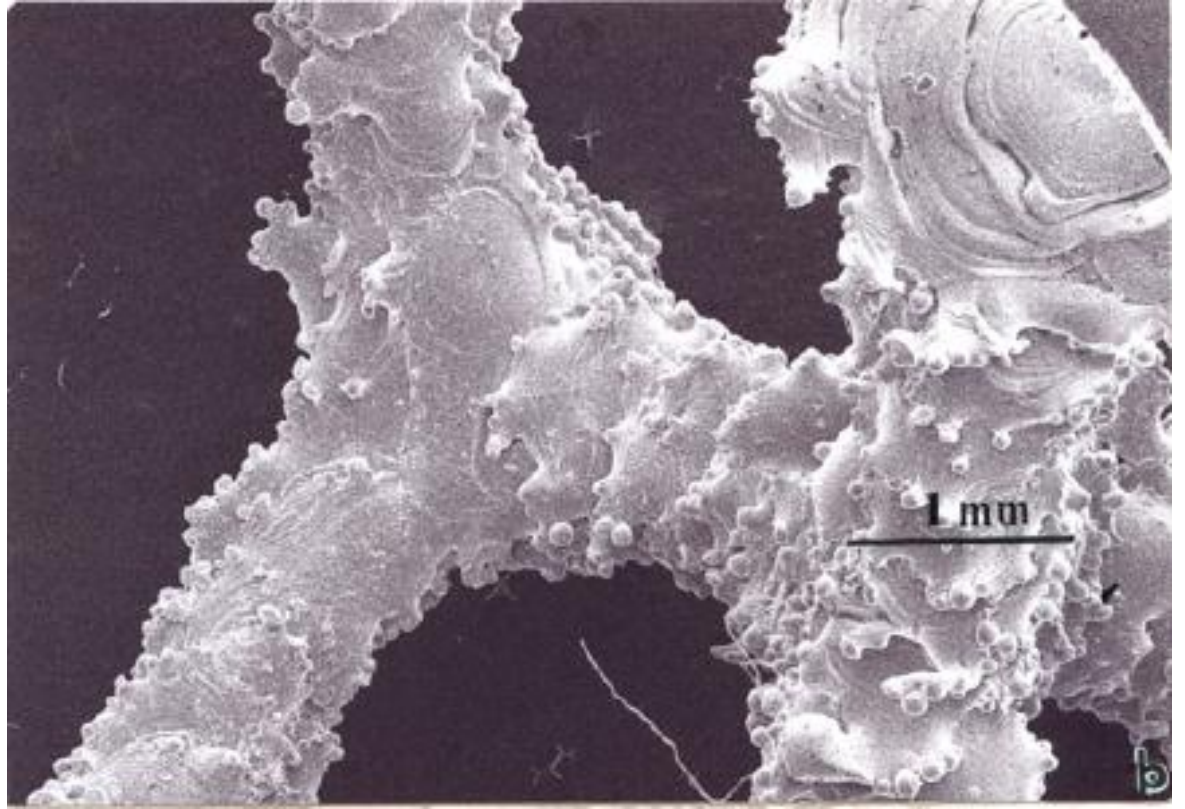
Figure 2.4: SEM image of the notched surface morphology in the porous region of a sample implant created using the electron beam melting (EBM) method [19].

Chapter 3

Previous Work on the Proposed Process

This chapter provides a brief description of previous work on the EDM pore-production process which is the subject of this investigation, as well as the results obtained from this work.

3.1 Description of the EDM Process

This investigation considers a *subtractive* route to major mechanical interlocking in an implant, in which a sub-surface-continuous pore structure is excavated from a pre-existing implant material using electrical discharge machining (EDM). This process places the material to be machined in a dielectric media after electrically connecting it to a tooling electrode. The tool electrode is brought close enough to the material to cause dielectric breakdown, and a small amount of material is removed through a thermal/evaporative process. With a sufficiently fine wire electrode, deep pores can be eroded into the material in this way. A schematic of how this would be implemented in an implant material is shown in Figure 3.1. This technique offers the advantage that automated EDM stations are more widely available in industry compared with the specialized equipment required by the rapid prototyping techniques. It also can be done at ambient pressure with no danger of causing extreme oxidation of the implant, saving the expense and difficulty of maintaining high vacuum. Moreover, preliminary investigations of this technique by Ankem *et al*. revealed that continuous pore clusters could be machined on a commercially-available titanium alloy common in prosthetic

implants. This process negligibly altered the alloy's grain structure and imparted a fine, undulating texture to the pore walls with RMS roughness on the order of 1μm. The negligible change in microstructure indicates that this technique can be utilized with thermomechanically processed materials to their full effect, while the fine roughness implies fewer sites for fatigue crack growth. This technique can also be used in tandem with other processes such as thermal oxidation or plasma spraying of interface layers for possible synergistic improvements in the bone/implant interface.
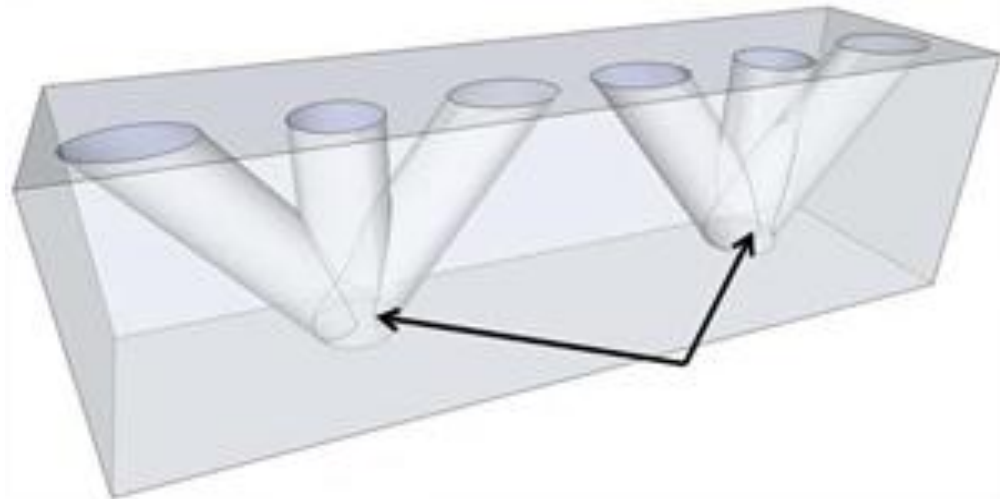
Figure 3.1: Schematic of an implant material containing surface pores which have sub-surface continuity machinable by EDM. The arrows indicate intersections between the pores. This EDM process was invented by S. Ankem (2008) and is being patented through the University of Maryland (U.S. patent application 12/754309), used here with permission.

While the proposed EDM process has several potential advantages over current methods of producing major mechanical interlocking at an implant surface, it does have a few technical shortcomings compared with rapid prototyping techniques related to the pore geometries achievable. For example, because pores must be machined from the

surface of the implant inwards by an electrode of fixed shape, architectures containing curvilinear pores, pores which change directions within the implant, pores which change diameter, and other possible design features cannot be produced. In addition, pores with multiple intersections deep within an implant are certainly possible, but require tight machining tolerances and might potentially be difficult at the production scale, whereas EBM and similar techniques have proven to be effective at this design feature.

3.2 Previous Work Done

3.2.1 Titanium Sample Preparation

The Grade 4 commercially pure titanium used in this investigation was purchased in the form of 1.25cm diameter bars from RTI International Metals, Inc. in Niles, Ohio. The bars were sectioned into disks approximately 0.5-2mm in thickness using a Buehler Isomet Low Speed Saw with diamond wafering blade. Buehler Isocut® fluid was used to lubricate and cool the wafering blade while removing debris, and a saw speed of 5 was selected. Cutting speeds were kept low to prevent sample damage due to cutting forces. Once one disk was cut from the bar stock, the thickness of the following disk could be selected by moving the sample holder a set distance in relation to the blade. This is accomplished by dialing in the attached micrometer the desired displacement. Eighteen divisions of the micrometer yielded specimens of approximately 120μm thick.

3.2.2 Electrical Discharge Machining of Pores

Pore fabrication was done by Optimation Inc. in Midvale, Utah. A wire EDM process was used with Commonwealth Supreme oil as the dielectric media. Arrays of

100-121 pores were machined into each sample, with diameters ranging from 180-250μm depending on the sample. Some samples had pores machined entirely through the thickness of the disk, while in other samples the pores were terminated inside the disk at a depth of ~600μm depending on the sample. Samples were prepared with intentionally non-interconnected pores as well as interconnected pores.

3.2.3 Thermal Oxidation

Two of the samples were intentionally oxidized, as creating a thick, rough surface layer of TiO_2 is one common method of improving the bioactivity and adhesion of titanium implants. Consequently, the response of cells in oxidized EDM-produced pores is important to study. The selected samples were held in a Lindberg type 51542 furnace under forced O_2 gas for 1 hour to achieve the desired oxidation.

3.2.4 Characterization of Pore Structures and Grain Size by SEM

To verify the grain size of the titanium material used and the interconnectivity of the pores produced, and also to examine the microstructure evolution resulting from the EDM process, the samples were examine in a scanning electron microscope (SEM). A Hitachi S-3400N SEM was used for this examination.

Using an additional pore machined into the side of one sample for the purpose of examining interconnectivity, it was confirmed that multiple pores can be made to intersect within the sample, as seen in Figures 3.2 and 3.3. In addition, the average grain size in the un-machined portion of the titanium was measured to be ~20μm. The average grain size within the machined region was virtually identical to that in the un-machined

region, demonstrating negligible modification of the material's microstructure during the

wire EDM process. It is therefore expected that the porous material created by EDM will

retain the mechanical properties (at the microscopic level) of the initial bulk material.
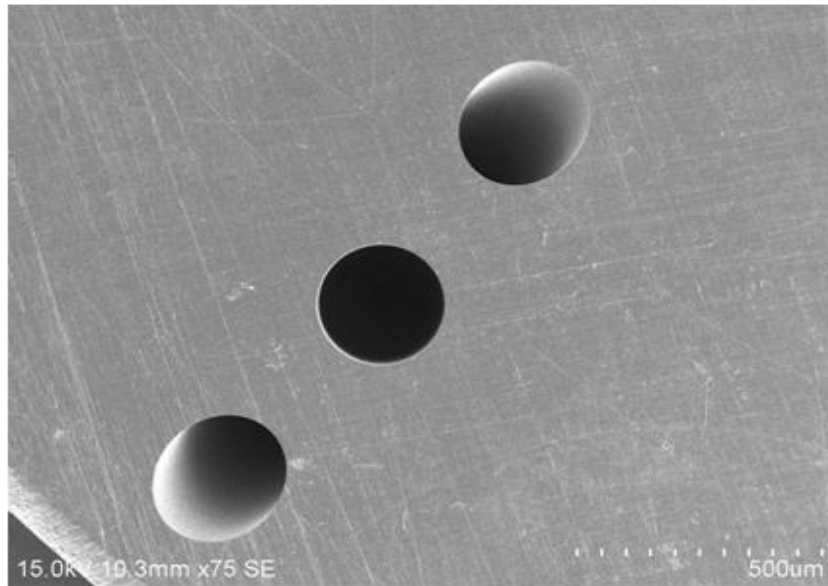
Figure 3.2: Face-on SEM image of intersecting angular and perpendicular pores
machined by EDM into the surface of a Grade 4 titanium sample.
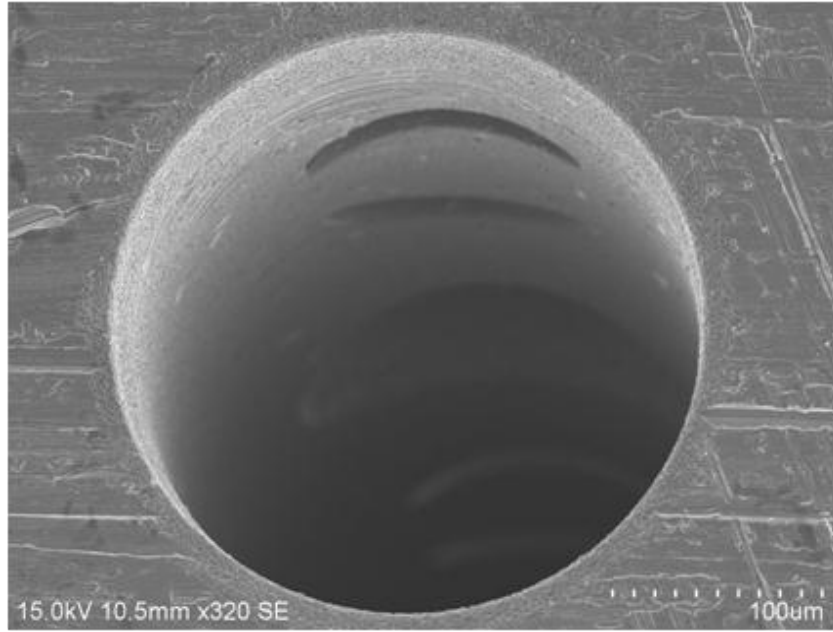
Figure 3.3: SEM image of a pore machined by EDM into the surface of a titanium sample, intersecting with several other pores beneath the sample surface.

3.2.5 Pore Wall Roughness Measurement by AFM

In order to assess the pore wall roughness created by the EDM process, a small, relatively flat portion of a pore wall was sectioned and prepared for topological mapping via atomic force microscope (AFM). An example of the results is shown in Figure 3.4. The surface was found to have an RMS surface roughness of approximately 1µm.
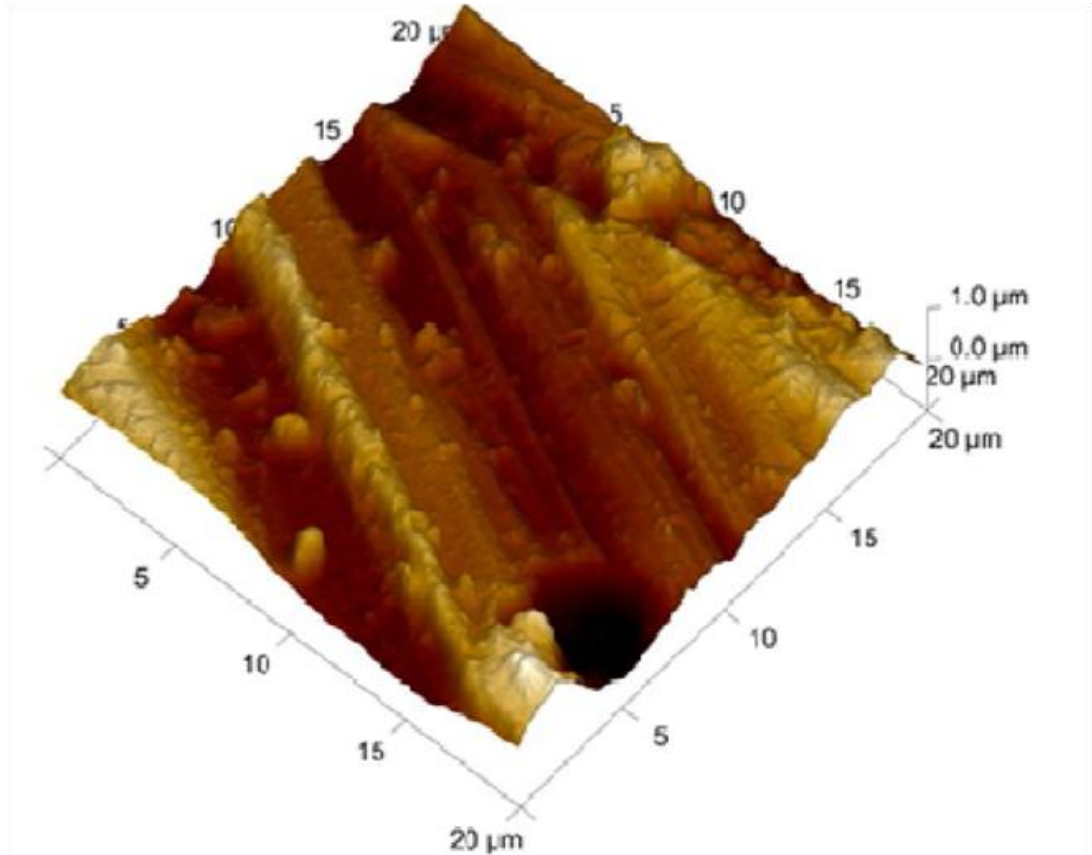
Figure 3.4: AFM image of the surface of one of the titanium samples which was intentionally oxidized. Surface roughness is ~1µm.

Chapter 4

Studies on Cell Proliferation and Mineralization in High-Aspect-Ratio

Pores Produced by EDM

As has been explained in the previous chapters, a highly porous implant surface which allows for major mechanical interlocking with the surrounding bone offers potential advantages in terms of mechanical strength and stress transfer at the bone/implant interface. However, these advantages can only be realized if the implant surface remains biocompatible, i.e. growth of healthy bone into this porous structure can be initiated and sustained at a level high enough to allow for major mechanical interlocking. In general, titanium alloys containing non-toxic alloying elements have been shown to be bioinert or bioactive, although the specific surface processing of the implant can have a significant effect on cell adhesion and proliferation. Implants possessing general surface roughness created by the EDM process have demonstrated favorable cell adhesion and viability when compared with other implant surface treatments [61]. Reports on other methods of creating interconnected porosities in titanium implants (e.g. through metal foams and rapid prototyping) also demonstrate significant bone ingrowth [59, 62]. However, no reports could be found in the literature on the response of bone-forming osteoblasts to the combined effects of the EDM process and deep, high-aspect-ratio pore structures, with or without sub-surface continuity. In principle, the combination of these implant qualities may affect bone ingrowth in unexpected ways, and so an assessment of cell viability on highly-porous titanium implant material created by the EDM method is necessary so that this processing

technique can be weighed against other methods. With this in mind, an investigation of the cell survivability, proliferation and mineralization in highly-porous EDM-processed Grade 4 titanium samples was conducted.

Unfortunately, budget constraints prevented the fabrication of large numbers of samples with sub-surface pore connectivity; these samples are more costly to machine compared with samples that have no pore connectivity when done in small, custom batches. The few samples which could be prepared having sub-surface pore continuity were used in preliminary cellular studies, and it was deemed best practice not to reuse these samples after cell fixation and staining had been done because of the risk of contamination to future cell batches. Consequently, the full effect of EDM-produced pore interconnectivity on cell viability has not been reported here. However, given the results reported here and literature reports on cell viability in continuous pore structures, it seems increasingly likely that cell proliferation and mineralization in EDM-produced continuous pores will also be satisfactory.

4.1 Procedures Followed

4.1.1 Cell Seeding of Samples

To conduct this experiment, the EDM-prepared titanium samples were first autoclaved to ensure sterility, pre-wet with ethanol, rinsed in phosphate-buffered saline (PBS), and placed in a 24-well plate. Then, bovine mesenchymal stem cells (MSCs) were seeded onto the top (machined) surfaces of the samples. The MSCs were purchased from Lonza Group of Walkersvile, Maryland. To perform this seeding, a cryovial of high passage bovine mesenchymal stem cells was thawed and suspended in 5mL of

temperature equilibrated culture media. The media used was Gibco culture media, which consists of high flucose DMEM, FBS, PEN/strep, non-essential amino acids, and L-glutamine. After a centrifugation and re-suspension in media, a cell count was taken and the cells (about 1 million total) were added to two T75 cell culture flasks with 20mL of media. The cells were then allowed to grow in an incubator for approximately three days. After cell growth was completed, one culture flask was examined under the microscope to ensure its cells were alive and growing. After this was confirmed, the media was extracted from the flask and a small volume of PBS was used to rinse the cells and any remaining media from the flask. Next, 3.75mL of temperature-equilibrated trypsin (used to cleave any bonds that the cells have with the surface of the cell culture flask) was added to the flask, which was then held at room temperature for 5 minutes. Once the cells had detached (as verified by looking under the microscope at the flask walls), the trypsin was neutralized with 3.75mL of media. The volume of cells was then mixed and transferred to a falcon tube, where it was centrifuged in order to isolate cells. The cells were then re-suspended in new media, and 1mL of the cell-filled media was added to a plate containing a titanium sample. Eight samples were prepared with cells. One mL of cell-free media was also added to each plate, and the media was changed every two days. The cells were deemed ready for preliminary viewing after approximately seven days.

4.1.2 Live/Dead Assay and Fluorescence Microscopy

After seven days, three of the samples were subjected to a live/dead assay. This process makes cells which are living at the time of the staining glow a fluorescent green

when viewed under a fluorescence microscope. Performing the live/dead stain involves submerging the samples in a solution of 100mL calcein acetoxymethyl/ethidium homodimer-1 and a fluorescent reagent for several minutes. Following the assay, the samples were transferred to glass slides and imaged using a Zeiss Axiovert 40 CFL fluorescence microscope. Results of this microscopy are shown in Figures 4.1 and 4.2. It can be seen that a minimum of one layer of cells (appearing green in the figures due to the live/dead assay) remained alive on the sample surface after seven days. In addition, the images suggest that the pores had become at least partially filled with pores during this time. This is due to the more intense fluorescence occurring within the pores (suggesting the presence of more cells) and the seeming absence of cells directly on the rims of the pores (suggesting the cells did not bridge over the pores instead of filling them). Cells filling the pores instead of bridging them would indicate the biocompatibility of the porous region. While these findings point to the biocompatibility of the EDM-created pores, the results are slightly ambiguous because of the resolution and perspective limitations of the technique, necessitating further study. With this in mind, cell proliferation was maintained on the five remaining untested samples for an additional 11 weeks, with media changes being administered every three days. This allowed for thorough mineralization to occur within the matrix secreted by the cells.
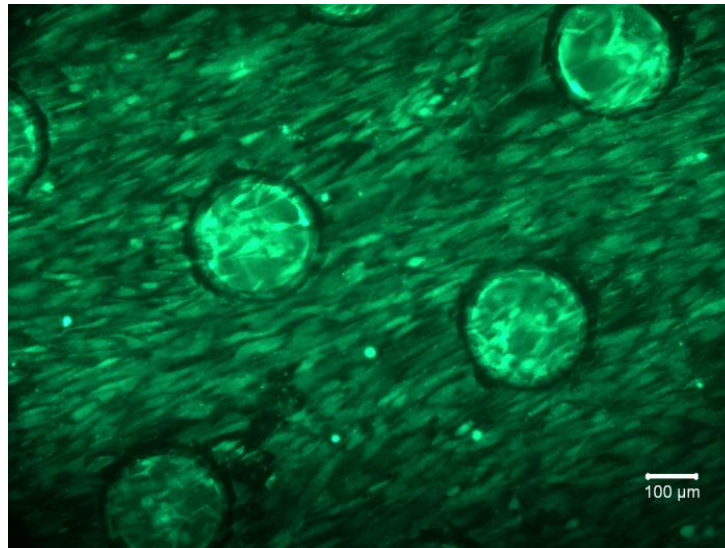
Figure 4.1: Fluorescence microscopy image of live/dead stained cells on the top (seeded) surface of a sample with perpendicular 250 μm pores terminating within the sample. The higher intensity of fluorescence inside the pores, and the apparent absence of cells at the pore border, indicate that cells are coating the walls and bottoms of the pores rather than bridging the tops of the pores.
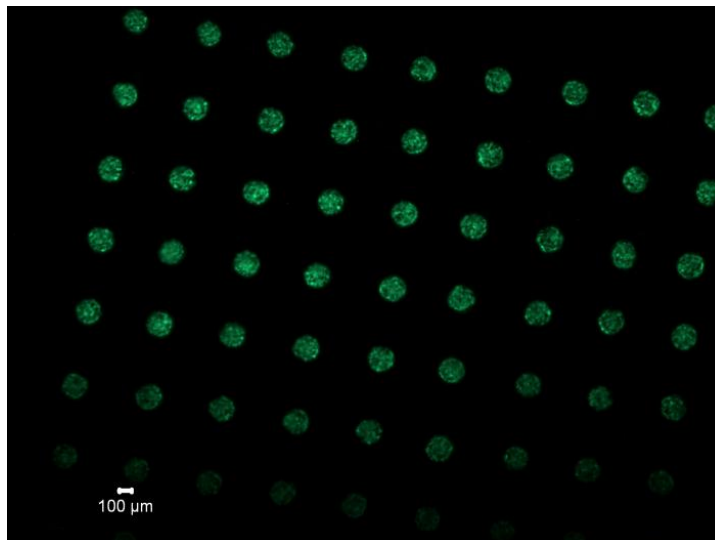
Figure 4.2: Fluorescence microscopy image of live/dead stained cells on the bottom (unseeded) surface of a sample with perpendicular 200 μm pores traversing the entire sample. While this image does not confirm that cells are coating the walls of the pores as opposed to bridging the top surface of the pores, it is thought that the observed fluorescence intensity is too high to be seeing only cells from the opposite end of the pores. Cells may be filling the entire volume of the pores, but are more likely simply coating the walls with a few monolayers of cells, and the fluorescence intensity is still high enough to give the appearance of full pore filling.

4.1.3 Cell Fixing

After the full 12 week period had passed, the samples were chemically fixed so that the biological tissue could be observed over longer periods of time without degrading. Fixatives generally accomplish this by crosslinking molecules within the biological tissue and by stabilizing proteins and other substances in the tissue against dissolution and decay. The samples were fixed in 4% paraformaldehyde and 0.1M sodium cacodylate buffer containing 10mM $CaCl_2$ at pH 7.4 at 4°C for 4 hours. Following fixation, the disks were placed in cassettes and washed with 0.1M sodium cacodylate buffer and 10mM $CaCl_2$ at pH 7.4 at room temperature for 24 hours.

4.1.4 Embedding of Samples in Polymethylmethacrylate (PMMA)

Following cell fixing, the titanium samples were embedded in polymethylmethacrylate (PMMA) in order to preserve and stabilize the biological structures on the samples over long periods. This embedding was done using a Heraeus Kulzer Technovit 9100 NEW PMMA kit, by following the directions included with the kit in combination with standard histological embedding protocols. The kit was used in the undestabilized state.

Prior to embedding, samples must be dehydrated. This was done by soaking the samples in the following progression of ethanol solutions: 40%, 50%, 60%, 70%, 95%, 100%, 100%, and 100%. The samples were gently stirred in each solution for 15 minutes. Following this, the samples were stirred in two baths of Citrisolv and two baths of xylene, for 15 minutes each, to complete the dehydration process.

Next, the samples were pre-infiltrated in preparation for PMMA embedding. First, the samples were stirred in a 50/50 solution of methylmethacrylate (MMA) monomer and xylene for 1 hour. Next the samples were moved to a bath containing 200mL of MMA monomer and 1g of dibenzoyl peroxide for 1 hour. Following pre-infiltration, the samples were infiltrated with a solution containing 250mL MMA monomer, 2g of dibenzoyl peroxide, and 20g of PMMA powder for 1 hour. During the infiltration process, the two components which react when combined to create the PMMA ("stock solution A" and "stock solution B") were prepared. Stock solution A consisted of a solution of 500mL of MMA monomer, 4g of dibenzoyl peroxide, and 80g of PMMA powder. Stock solution B consisted of a solution of 50mL of MMA monomer, 4mL of N,N,3,5-tetramethylaniline, and 2mL of 1-decanthiol. Solutions A and B were combined in a 9:1 ratio and stirred until well mixed to begin the polymerization process. The titanium samples were placed in disposable containers and the polymerization mixture was poured on top of the samples until they were covered. The samples were then placed in a sealed container and stored in a -20°C freezer as per the manufacturer's instructions. Polymerization progressed more slowly than expected, and so after approximately 48 hours the samples were removed from the freezer and stored at room temperature until the PMMA had become fully solidified.

4.1.5 Removal of Polymethylmethacrylate (PMMA) from Samples

Immediately prior to microscopy observations done on the titanium samples, the protective PMMA covering was removed so that it did not obscure features of the samples. A chemical removal process was used, although it was found that mechanically

removing the majority of the PMMA through cutting and sanding greatly expedited the removal process without producing adverse effects in the samples. Once the PMMA had been trimmed down to approximately 1mm in thickness, the samples were gently stirred in three baths containing approximately 150mL of 2-methoxyethylacetate (2-MEA) for 20 minutes each, as recommended by the PMMA manufacturer, and were then visually inspected. If any visible PMMA remained, the samples were soaked an additional 1-2 times in 2-MEA, again for 20 minutes each. This removed all traces of the PMMA covering.

4.1.6 SEM Examination of Samples

The samples were examined using scanning electron microscopy (SEM) after 12 weeks of growth to visually assess the extent of cell proliferation and mineralization within the pores. In addition, energy dispersive x-ray spectroscopy (EDS) incorporated with the SEM was used to determine the elemental composition of the mineralized matrix produced by the cells. A Hitachi S-3400N SEM was used for this examination.

Results of this examination are shown in Figures 4.3 and 4.4. Out of the five samples examined, only two showed signs of cell ingrowth and mineralization; the rest showed virtually no chemical buildup on the commercially pure titanium, as seen in Figure 4.3. However, the mineralized matrix production was quite extensive on the two samples which exhibited it. Approximately 88% of the pores on these samples were at least partially filled with matrix material. Example images of this material are shown in Figure 4.4 and 4.5. The samples showing mineralization had dissimilar properties (one was bare titanium with pores traversing the entire disk, while the other was thermally

oxidized and had pores terminating inside the sample), suggesting that none of these properties contributed to cell death or inactivity on the samples which showed no mineralization. All samples were incubated in different wells of the same 24-well container, and received the same treatments at the same time, so the reasons for lack of matrix production on three samples are unclear at present. It could be possible that a pathogen attacked the bare samples but was unable to propagate to the mineralized ones, or the bare samples may have been contaminated by some unidentified substance which was removed during the depolymerization process.
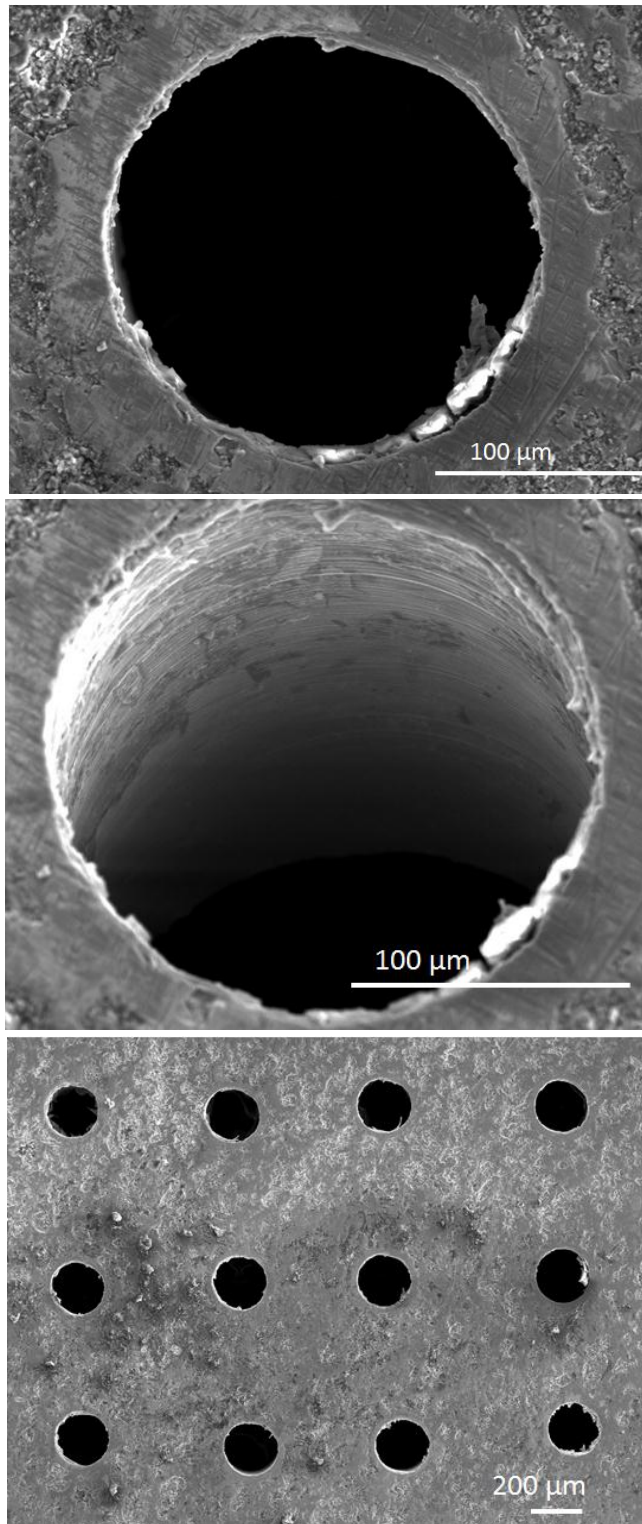
Figure 4.3: (Top) Face-on view and (Center) angled view in the scanning electron microscope of a 200µm diameter perpendicular through-cut pore on a titanium sample which did not exhibit signs of mineralized matrix. (Bottom) Image from the same sample showing multiple pores.
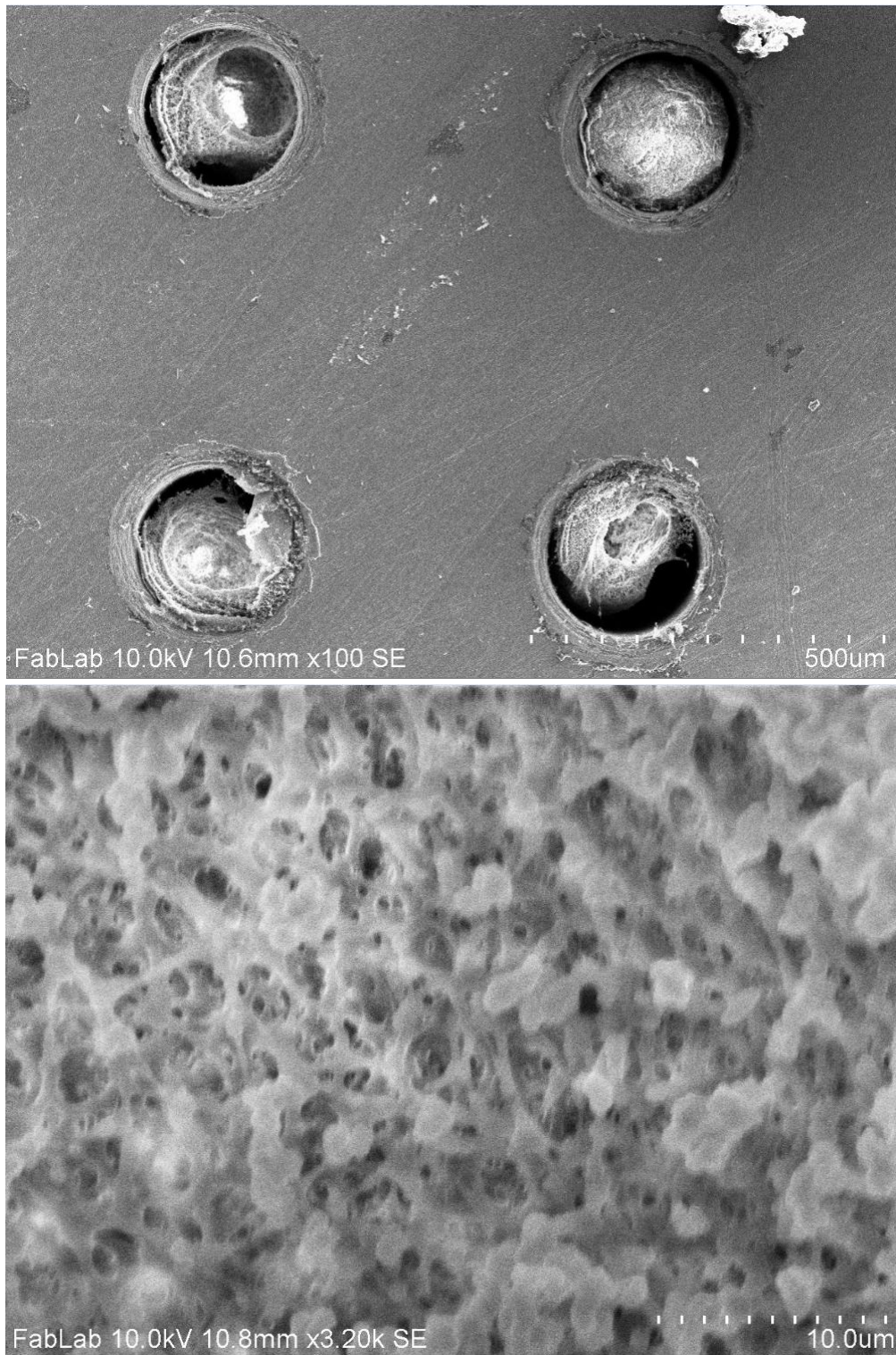
Figure 4.4: (Top) secondary electron image details of mineralized matrix filling the pores of an intentionally oxidized specimen. (Bottom) Close-up of the mineralized matrix within one of the pores.
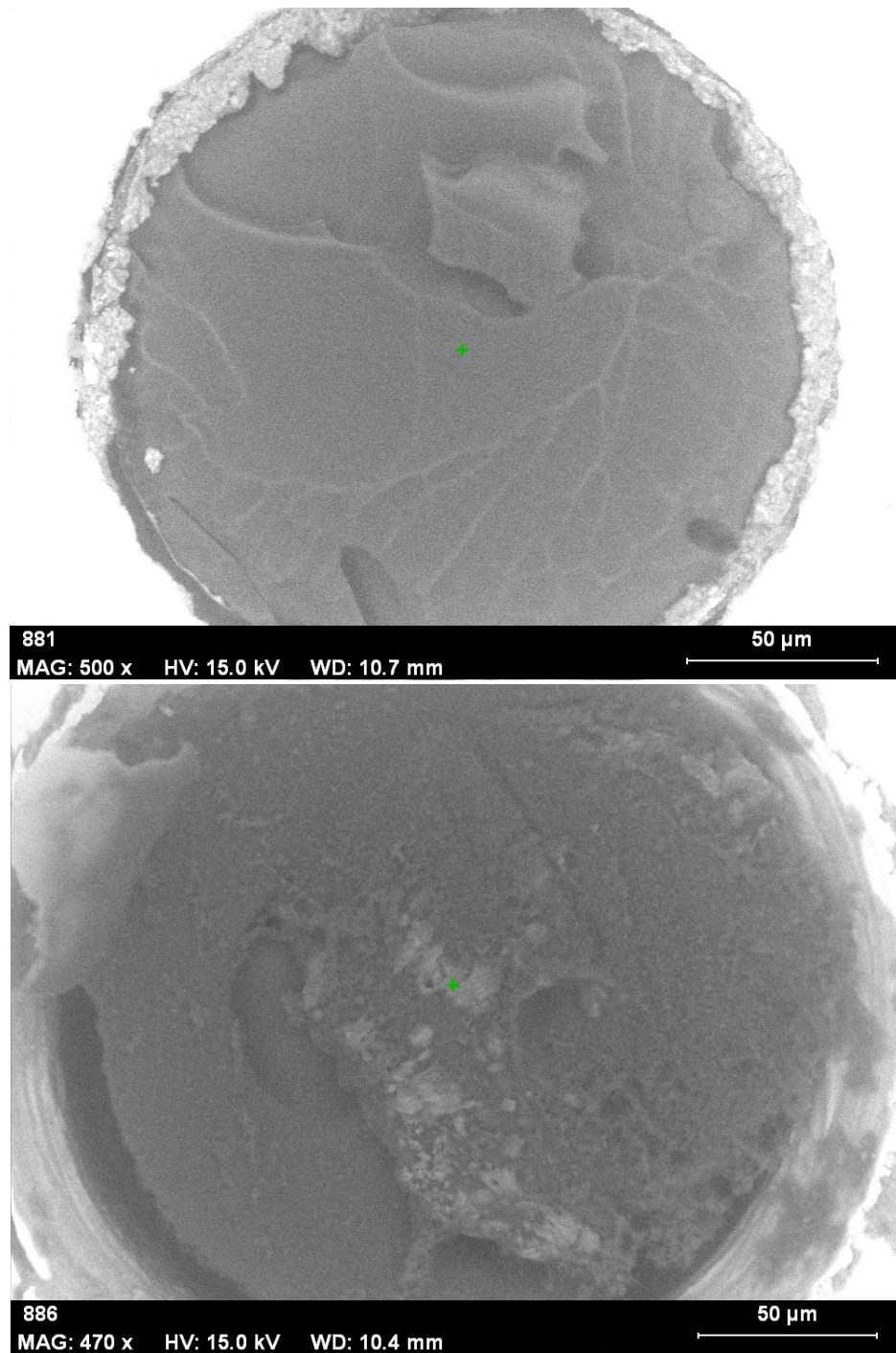
Figure 4.5: (top) SEM picture of mineralized matrix (grey, center) filling a 200μm diameter perpendicular through-cut pore on the surface of a titanium sample (white, periphery). (Bottom) SEM picture of mineralized matrix filling a 200μm diameter perpendicular pore terminating in the center of an intentionally oxidized titanium sample. In both images, EDS spectra were taken centered at the green crosshairs.

To assess the extent of mineralization in the matrix material that was found, EDS spectra were taken on various points on the matrix. Examples of these spectra are shown in Figures 4.6 and 4.7. In addition to the measurement of titanium from the disk itself, the carbon, oxygen, calcium and phosphorus readings are all consistent with the composition of mineralization found in bone. For all spectra, the ratio of calcium to phosphorus (in terms of atomic percent present) was determined, as shown in Table 4.1. The average calcium-to-phosphorus ratio was found to be 1.45, which indicates that a significant amount of mineralization has occurred. The initial calcium-to-phosphorus ratio in bone-forming osteoblasts is quite low, and calcium accumulates as mineralization occurs until this ratio approaches ~1.63 in normal bone [63]. EDS was performed on the bare titanium samples as well, to confirm that there were not chemical compounds adhering to the surface following depolymerization which were interfering with measurements of the matrix material. Titanium and oxygen were the only observable elements in these spectra, indicating that no such chemicals were present. In addition, a spectrum was taken on a piece of polymethylmethacrylate which was removed from one of the samples prior to depolymerization. This was to verify that the spectra obtained inside the pores was coming from mineralized matrix and not any remaining traces of polymethylmethacrylate on the sample which had been impregnated by calcium and phosphorus from the cells or cell media. This spectrum revealed that only carbon and oxygen were present in significant amounts, as expected (see Figure 4.8).
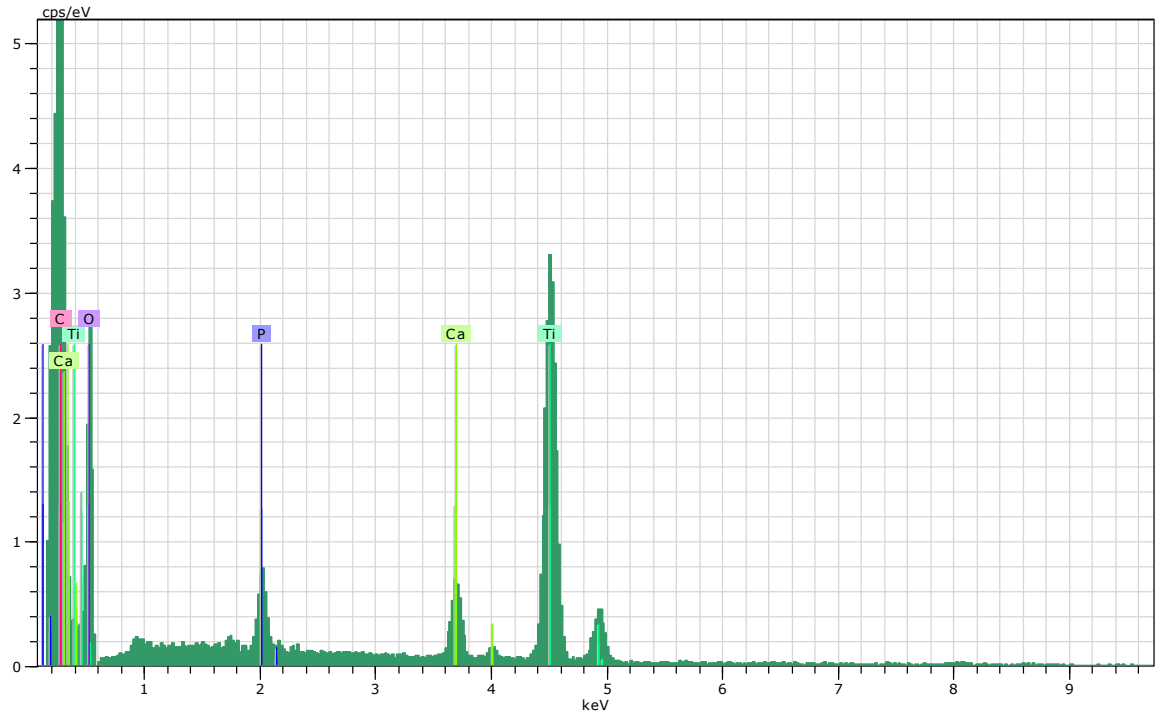
```
Spectrum: _1 3602

El AN  Series   unn. C norm. C Atom. C Error
                [wt.-%] [wt.-%] [at.-%]   [%]
-------------------------------------------------
Ti 22 K-series   33.29   34.22   13.94    1.0
C   6 K-series   23.54   24.20   39.31    3.2
Ca 20 K-series    3.63    3.73    1.81    0.2
P  15 K-series    2.00    2.06    1.30    0.1
O   8 K-series   34.82   35.79   43.64   39.8
-------------------------------------------------
       Total:    97.28  100.00  100.00
```

Figure 4.6: (Top) EDS spectrum obtained at the green crosshair in the mineralized matrix filling a 200μm diameter perpendicular through-cut pore on the surface of a titanium sample. (Bottom) Numerical results of the EDS analysis.
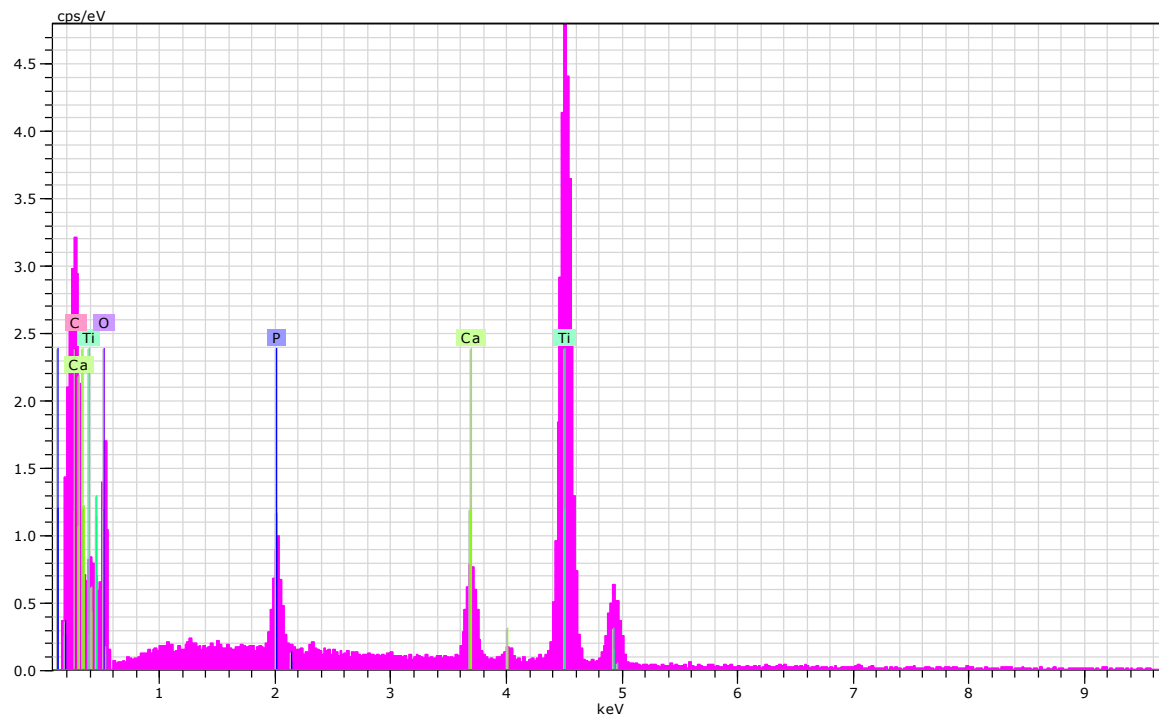
```
Spectrum: _1 3607

El AN  Series   unn. C norm. C Atom. C Error
          [wt.-%] [wt.-%] [at.-%]   [%]
----------------------------------------------
Ti 22 K-series   55.09   53.69   27.75   1.7
C  6  K-series   13.56   13.21   27.22   2.0
Ca 20 K-series    4.28    4.17    2.58   0.2
P  15 K-series    3.11    3.03    2.42   0.2
O  8  K-series   26.57   25.89   40.04  37.3
----------------------------------------------
      Total:  102.60  100.00  100.00
```

Figure 4.7: (Top) EDS spectrum obtained at the green crosshair in the mineralized matrix filling a 200µm diameter perpendicular pore terminating in the center of an intentionally oxidized titanium sample. (Bottom) Numerical results of the EDS analysis.

Table 4.1: Calcium-to-phosphorus ratios measured on different areas of the samples showing mineralization, as measured by EDS.

Sample	Measurement	at% Ca	at% P	Ca/P ratio	Ca/P ratio (total average)
#1 (unoxidized surface, through-cut perpendicular pores)	1	2.14	1.7	1.258824	1.44715776
	2	1.73	1.51	1.145695	
	3	1.81	1.3	1.392308	
	4	8.28	2.75	3.010909	
#2 (oxidized surface, perpendicular pores terminating in sample)	1	1.56	1.14	1.368421	
	2	0.95	0.75	1.266667	
	3	5.16	4.83	1.068323	
	4	2.58	2.42	1.066116	
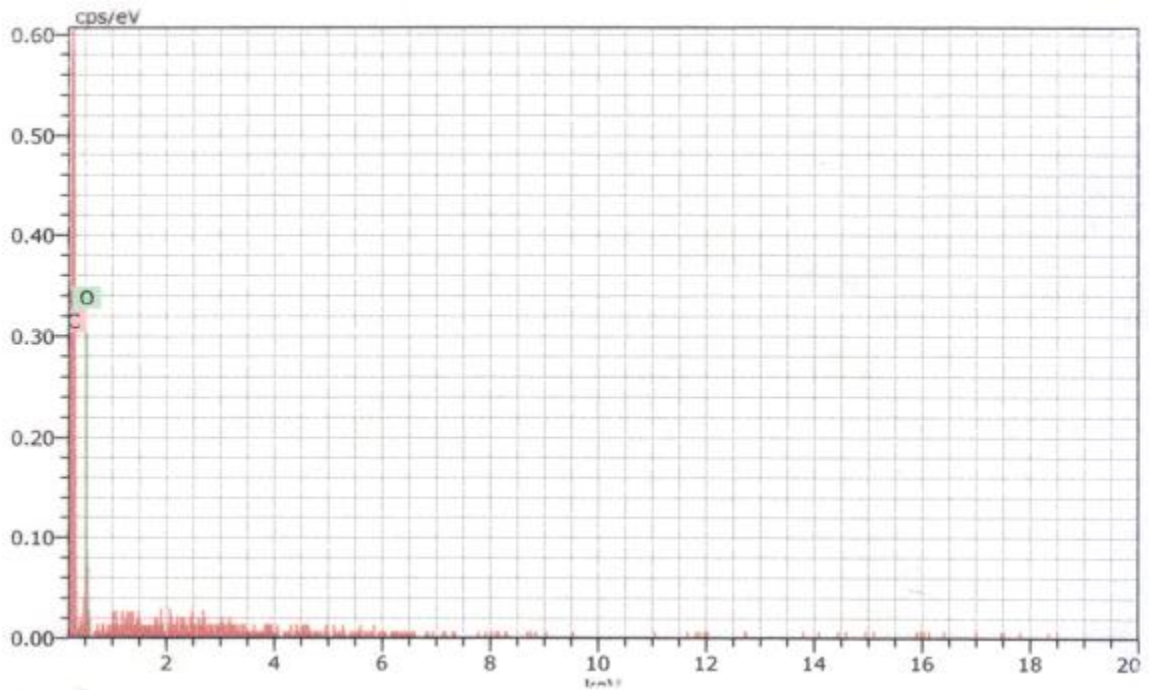
Figure 4.8: EDS spectrum of polymethylmethacrylate cut from a sample prior to depolymerization. The calcium and phosphorus peaks are absent, verifying that the spectra obtained from inside the sample pores is not produced by undissolved polymethylmethacrylate.

Although the SEM did not present a simple means of determining the depth of matrix production within the pores, observations can be made indicating it is more extensive than simply a mineralized bridge at or near the surface of the pores. For example, brightness contrast can be seen across some surfaces of the matrix within the pores, and this brightness correlates with the distance of the surface from the electron beam. This implies that in some cases, the matrix possesses a slanted or undulating surface, which would require non-uniform penetration of cells into the pore. In addition, pores could be found exhibiting only partial pore filling, as seen in Figure 4.9. In these pores, the sample stage could be tilted to show connectivity of the matrix with the pore wall at various depths, again demonstrating that cells penetrated an appreciable depth into the pore. For a more rigorous assessment of this penetration, additional characterization was needed, as discussed in the next section.
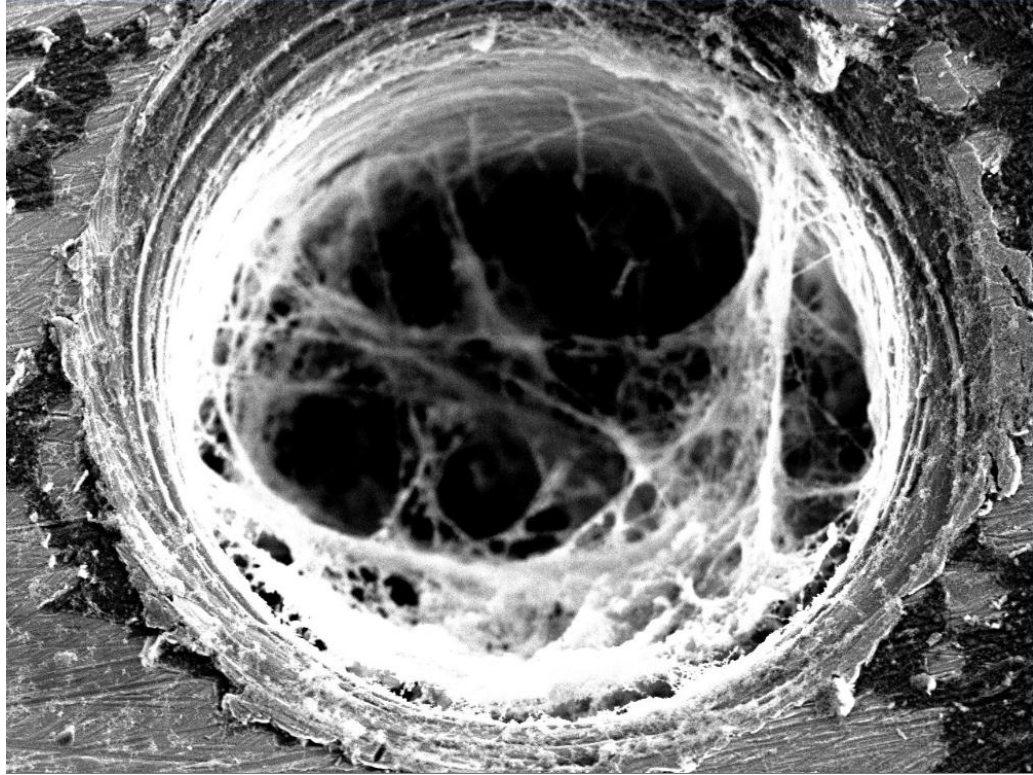
Figure 4.9: SEM image of a pore which has undergone only partial mineralization. The sample was tilted for this image to show the matrix connectivity at various points along the pore wall, demonstrating matrix penetration into the pore.

4.1.7 Confocal Microscopy of Samples

To determine the depth of penetration of mineralized matrix into the EDM-machined pores quantitatively, confocal microscopy was performed on a sample with through-cut perpendicular pores. (The confocal microscope used operates via transmission, so pores terminating within the sample could not be analyzed.). An Olympus IX81 confocal microscope was used for this investigation.

The sample was placed on a glass slide on the microscope stage and viewed at 100X magnification under white illumination. First, the pores which had failed to fill with mineralized matrix were quickly identified, and it was determined that these constitute approximately 12% of all pores on the sample. Next, for the pores which were

filled with matrix, the pore was centered in the viewing area and the surface of the matrix was manually brought into focus. Example images of the matrix surface are shown in Figure 4.10. The software associated with the microscope automatically determined the focal length of the microscope, and this was recorded when each pore was brought into focus. The sample was then turned over, the microscope was focused on the opposite side of the matrix, and this new focal length was recorded as well. Then, the two focal lengths corresponding to each pore were compared. Assuming that at least one surface of the matrix is very near to the surface of the sample (which is a good assumption based on the SEM images), then the depth of matrix penetration into the pore is equal to the sample thickness ($\sim$406µm) minus the change in focal length.
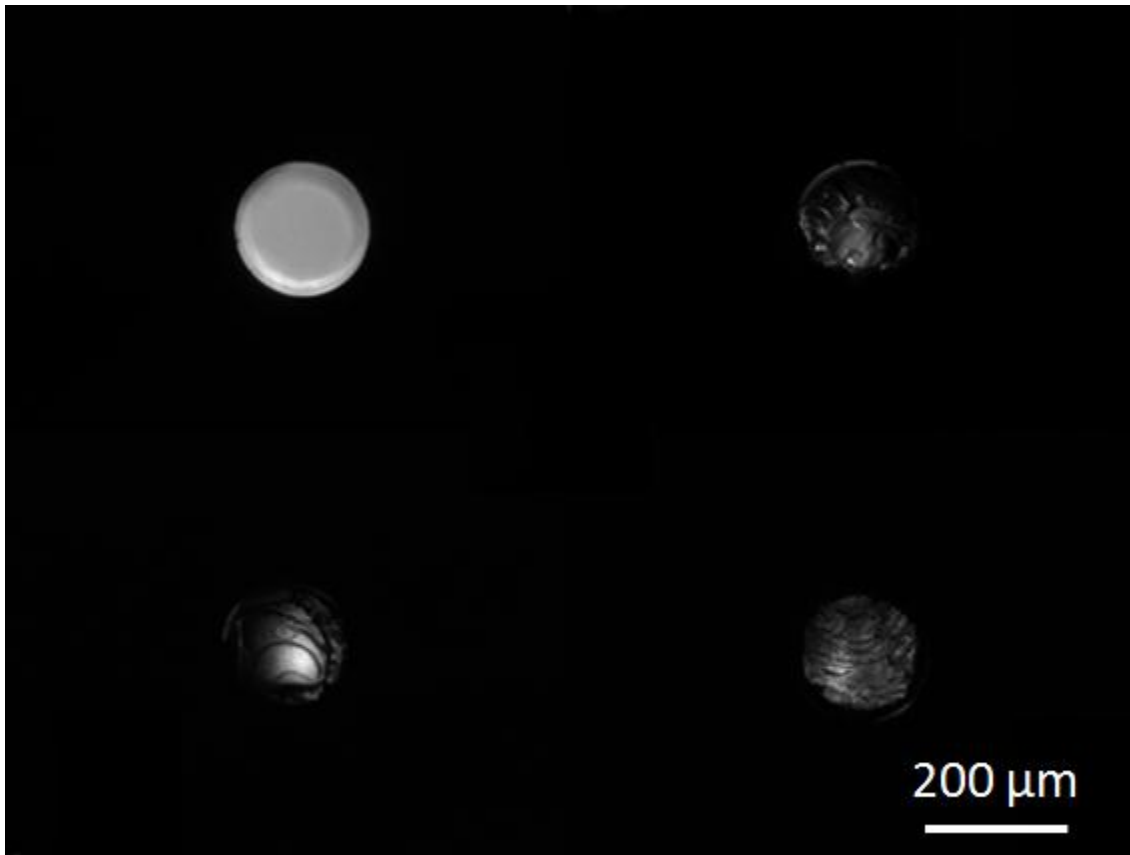
Figure 4.10: Confocal microscope images of an unfilled through-cut pore (top left) and other pores filled by mineralized matrix.

Of the pores measured, the average matrix penetration was found to be 303µm with a minimum of 226µm and a maximum of 387µm. These findings confirm that osteoblasts effectively propagate within the pores instead of bridging them, as in all cases the matrix thickness greatly exceeds the size of a single osteoblast (~30µm). Further, in several of the pores the matrix filling is essentially complete. (The thickness of the matrix and the depth of the pore differ by less than the size of one osteoblast, and this difference may come in part from measurement error or the removal of small amounts of matrix during sample depolymerization and handling.) This implies bone growth into deeper pores should occur as well, especially when vascularization and other *in vivo* processes beneficial to cell growth are present.

4.2 Conclusions

A study of the cellular response of bovine mesenchymal stem cells was performed on commercially pure titanium containing deep, high-aspect-ratio pores produced by the EDM method. The cells were seeded onto the samples and allowed to proliferate and mineralize for a total of twelve weeks. At the end of this growth period, it was found via SEM that selected samples exhibited significant ingrowth within the pore structure. EDS analysis indicated that the amount of mineralization within the matrix produced by the bone-forming cells approached that found in healthy bone. Confocal microscopy revealed that this mineralization extended an average of over 300µm into the pores, and often filled essentially the entire pore. This suggests that bone ingrowth could extend even further given deeper pores and beneficial *in vivo* conditions. These results were expected, given prior cellular studies on EDM-machined titanium surfaces and within

high-aspect-ratio pores produced by other methods. Several of the samples tested did not exhibit the desired mineralization; however, the total sample size was small, and it is predicted that continued studies would lead to a larger percentage of mineralized samples.

Chapter 5

Finite Element Modeling Studies of Pore Structures Machinable by EDM at the Bone/Implant Interface

Although the failure strengths of implant materials, various types of bone, and various types of interfaces between these two materials have been extensively studied, there has been less study of the bone/implant interface strength when major bone ingrowth within the implant has occurred. The mechanical properties of each material and each interface, along with the geometry of the interconnection between the two, result in an "interlocking strength" which is similar to a standard interfacial strength but in principle can greatly exceed the typical interface strength of bone and titanium. (For this investigation, the term "interlocking strength" is taken to mean the stress at which bulk material failure initiates in either titanium or bone, not the potentially higher stress at which the interface utterly fails. Small-scale separation at the interface between implant and bone is allowed to occur without failure, according to this definition). The ultimate strength of the bone/implant interface has been demonstrated computationally for certain porous implants [28], but interface geometry can greatly impact this strength. Since one of the most readily-identified shortcomings of the EDM process described herein is its geometric limitations when creating pores, the pore structures which it *can* produce must be examined to determine the resulting interface properties of this method.

Finite element modeling (FEM) is a powerful analytical tool for determining the mechanical behavior of single- and multi-material components in a variety of structural applications. By approximating a component of complex shape (in which stresses and

strains cannot generally be determined analytically) as a series of shapes or "elements" for which an exact solution to stresses and strains can be found, mechanical behavior of a component can be simulated with a high degree of accuracy. In these investigations, three-dimensional finite element modeling was used to study the stress distributions near the bone/implant interface when various EDM-machinable structures are present at the interface. It is the goal of this work to determine the interlocking strength for interfaces that are machined with these pores, and to examine the effect of pore orientation on interface strength. In addition, the pore structures must also promote good stress transfer from implant to bone, and resist unwanted separation that could accelerate the intrusion of wear particles in the interface. This investigation seeks also to assess qualitatively the interface separation occurring under approximately equal loading conditions, and the change in stress transfer from implant to bone when there is an interconnected vs. non-interconnected porosity of equal volume fraction at the interface. The FEM tool ANSYS [64] was used for this investigation.

5.1 Input Properties and Pore Geometries

In this investigation, the materials simulated (cortical bone and Grade 4 titanium) were assumed to have isotropic mechanical properties. The mechanical properties assigned to the different materials are given in Table 5.1, and were taken from literature values [26, 28, 65].

Table 5.1: Material properties used as input for the finite element simulations of this investigation [26, 28, 65]. The failure strengths of the bone/implant interface were chosen in an attempt to reasonably approximate the properties of a wide variety of surface treatments which can be used in conjunction with the EDM method. They are also only approximate values in that interface failure occurs gradually over a range of stresses in the Exponential Cohesive Zone Model used in this investigation.

Material	Young's Modulus (GPa)	Poisson's Ratio	Failure Strength (MPa)		
			Tensile	Compressive	Shear
Grade 4 Ti	105	0.3	480	480	480
cortical bone	6.8	0.3	47.5	150	51.6
bone/implant interface	N/A	N/A	~0.5	N/A	~4

It was assumed that the porosities produced by the EDM method for this investigation would be repeated units of an interconnected "pore cluster." The primary variables considered in the FEM analysis were the number and orientation of pores within each cluster. Literature reports on porous implants indicate that pore diameters in the range of 100-400μm result in optimal ingrowth of healthy tissue into the pores and resultant adhesion of the implant [53-57], and so all pores modeled in this investigation were given a diameter of 400μm. (Note that ANSYS assigns no units to the values inputted by the user; it is up to the user to ensure beforehand that the units of all inputted values are consistent. All length values input during this investigation were assumed to represent micrometers.) Prior work also indicates that bone ingrowth into a porous implant results in little added interfacial strength beyond a depth of 1500μm [28], so that was the maximum depth assigned to the pore structures in this study. Preliminary simulations suggested that an angle of inclination of 25° would produce reasonably high interlocking strengths while keeping computation times relatively low as well (due to the

shorter pore lengths and fewer elements needed to model them). Complete bone ingrowth within the porous models was assumed in all cases.

In this work, the "pore clusters" each consisted of one cylindrical pore machined into the implant with its cylindrical axis perpendicular to the implant surface, and other pores intersecting this perpendicularly-cut pore near its bottom at some angle, α. These angular pores were evenly spaced around the perpendicular pore (i.e. a pore cluster containing two angular pores and one perpendicular pore had rotational symmetry about the long axis of the perpendicular pore by rotating 180°, whereas a cluster with one perpendicular and three angular pores had the same symmetry at 120°). The perpendicular pore was included in all cases to minimize the distance of travel for cells and nutrients into the pore structure for a given pore depth, which is expected to promote better bone growth (and consequently strength) at the point of pore intersection. Larger and more complicated pore structures were not considered in this work, although they are certainly possible to produce with the EDM method and may improve mechanical and biological properties of the implant compared with the proposed structures.

5.2 Model Development

Two different model geometries were created for this work, depending on the objective. Specific instructions related to the creation of models within the ANSYS interface are included in the Appendices.

5.2.1 Model for Determining Interlocking Strengths

The first models produced aimed at stressing selected bone/implant interfaces until material failure occurred. For these models, a pore structure having a specific geometry was excavated from the face of a simulated block 5mm by 5mm by 2.5mm in size, which was assigned the material properties of Grade 4 titanium. For ease of comparison, the volume and amount of porosity/interconnectivity between the interfaces was held constant for each structure considered. Three pore structures were selected which fit this criterion while remaining computationally efficient: a structure of four intersecting pore clusters containing 2 angular pores (Pore Structure A), a structure of three pore clusters containing 3 angular pores (Pore Structure B), and 12 non-intersecting perpendicular pores. The angle of inclination α between each angular pore and the perpendicular pore was 25°. All three structures considered contained 12 machined pores, and the volume fraction of pores in each model was kept approximately equal. (A flat, non-porous interface was also considered.) The pore structure was filled with material having the properties of cortical bone, and this was attached to an adjoining block having the same properties, also 5mm by 5mm by 2.5mm in size. Examples of the finished structures (viewed as only the bone portion of the model) are shown in Figure 5.1.
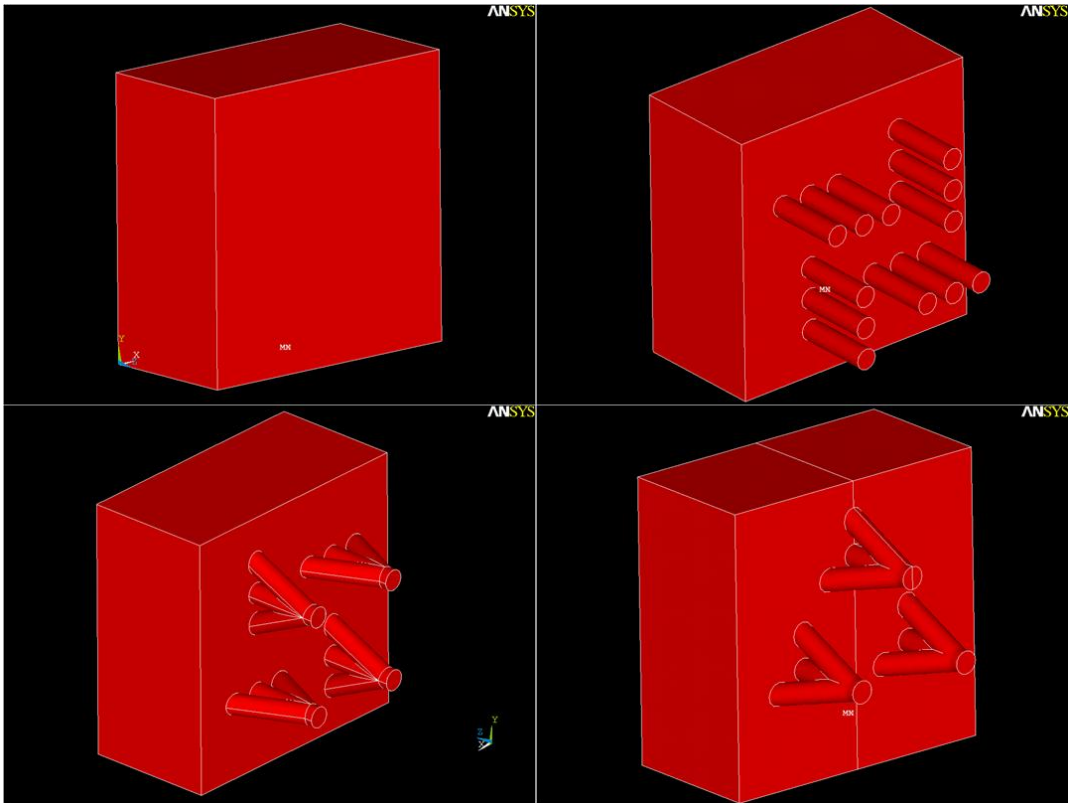
Figure 5.1: The different interfaces created for this investigation, viewed as only the bone portion of the model (the titanium portion is a similar block, with pores corresponding to the protrusions shown in the above pictures). Clockwise from top-left: flat (non-porous) interface, porous non-intersecting interface, porous intersecting structure "B", and porous intersecting structure "A."

Once the two blocks (interlocked by bone within the machined pore) had been created through the ANSYS interface, the models were meshed into nodes and elements. This was done automatically by the program using the Smart Size feature, with the mesh density varying based on the local complexity of the model (i.e. many small elements were created near the porous region of the implant, while fewer large elements provided sufficient accuracy far from the porous region). This resulted in a total element count of at least 80,000, which translated to an element density exceeding that deemed acceptable in similar works [28] in addition to satisfying in-house mesh density checks. The

49

quadratic tetrahedral element SOLID187 was used, which is appropriate for accurately modeling complex three-dimensional geometries.

Once the bone and titanium components had been meshed, the interface between them was defined. The bone/implant interface possesses characteristic tensile and shear strengths which are much lower than the strengths of either bone or titanium. These strengths vary widely based on test conditions and the type of implant surface present; for this investigation, an interface tensile strength of 0.5MPa and a shear strength of 4MPa were chosen in an attempt to approximately represent a wide range of interface conditions. To simulate these interface properties, an Exponential Cohesive Zone Model was used, which simulates gradual de-bonding at an interface using interface elements which soften exponentially with increasing displacement. This is one of the prescribed methods of modeling de-bonding within ANSYS, and serves to approximate interface behavior without producing sudden large changes in the model that can cause numerical instability. The input parameters for the Cohesive Zone elements were determined empirically by simulating tensile and shear stress on a flat (i.e. non-porous) interface. The chosen input parameters resulted in a gradual increase in the maximum stress acting in the implant up to an applied stress of approximately 0.5MPa and 4MPa in tension and shear, respectively. A precipitous drop in maximum stress in the model was seen for higher applied stresses, indicating interface failure. (The values of 0.5MPa and 4MPa are approximate because the gradual softening of the interface elements makes defining an exact stress at which the interface "fails" difficult.)

After meshing, boundary conditions and constraints were imposed on the model. The nodes on the back face of the titanium block (furthest from the bone/implant

interface) were constrained to be motionless in all directions, to simulate the rigid interior of a prosthetic. The nodes on the front face of the bone block, also furthest from the bone/implant interface, were allowed to move but were given a multi-point constraint: all nodes were required to have the same amount of displacement in the Z direction (perpendicular to the plane of the front face) at all times. This was again aimed at mimicking the bone far away from the bone/implant interface. An example of a fully assembled, meshed, and constrained model is shown in Figure 5.2.
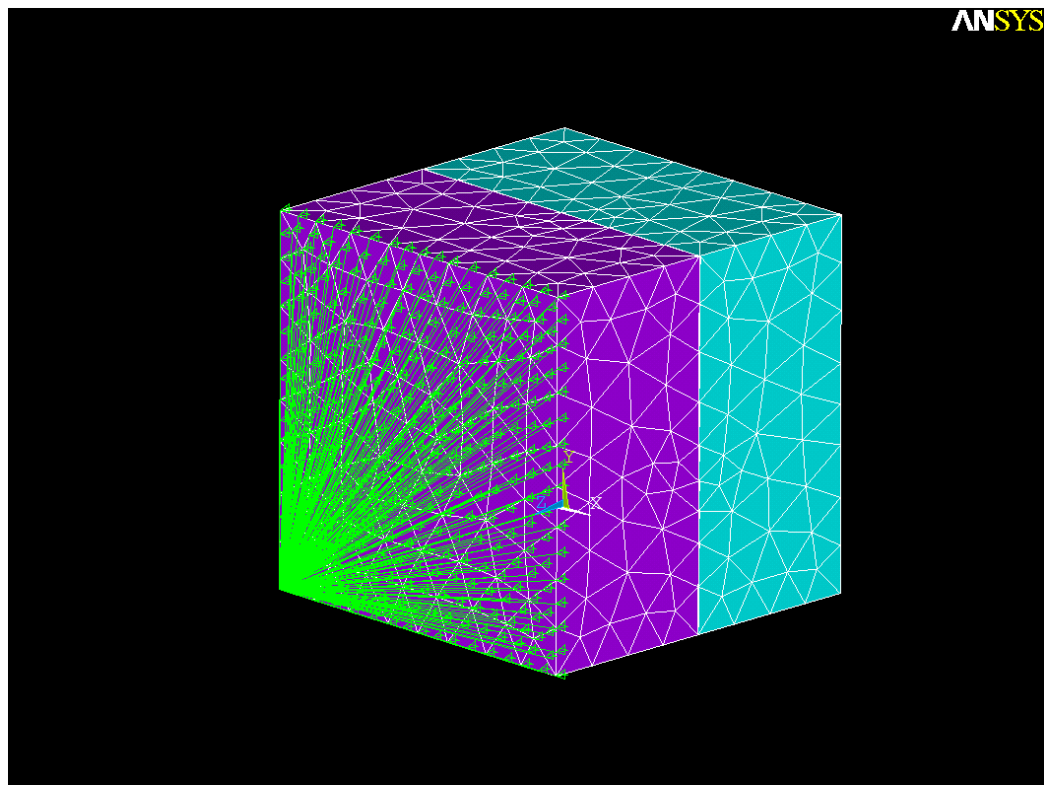
Figure 5.2: Meshed exterior of model used for FEM calculations. In this image, purple represents bone and teal represents titanium. The multi-point constraint on the front face of the bone along the Z-direction is indicated by the green lines.

After model boundary conditions were applied, loads were applied to the models as displacement. Displacements were used instead of force or stress because the use of

interface elements necessitated a non-linear analysis of the model, and displacements acting on the model were less likely to cause numerical convergence issues [64]. The displacement was gradually increased in an iterative process until a dramatic drop in stress was observed (for the model with non-intersecting pores) or until fracture initiated in the bone material. The Maximum Normal Stress Theory was applied to determine when fracture occurred; if the 1st principal stress in any element of the bone material exceeded the designated tensile strength (47.5MPa), failure was said to occur. The stress at which failure occurred was defined as the average stress in the loading direction among the nodes on the face to which the displacement was applied. Example images of the models during the loading process are shown in Figures 5.3 through 5.9.
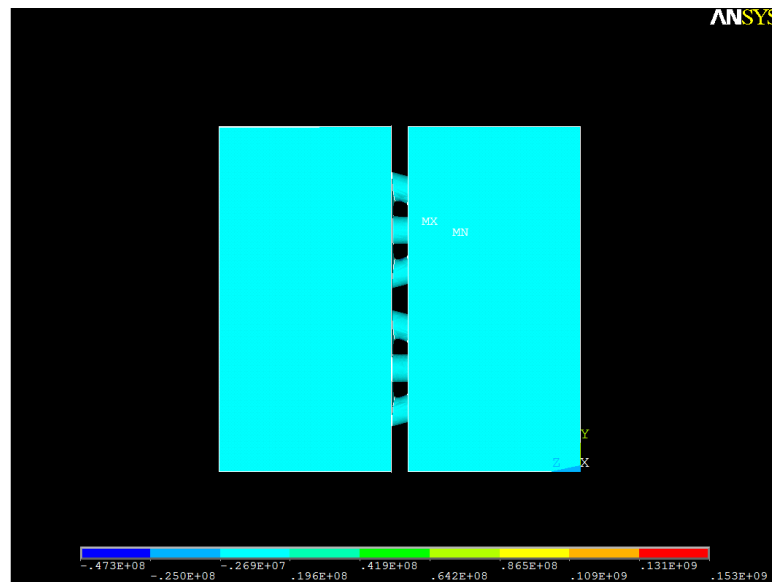
Figure 5.3: Plot of the 1st principal stresses acting in the interlocking strength model with Pore Structure A under tension near the point of failure (with interface elements graphically suppressed). Separation at the interface is graphically exaggerated.
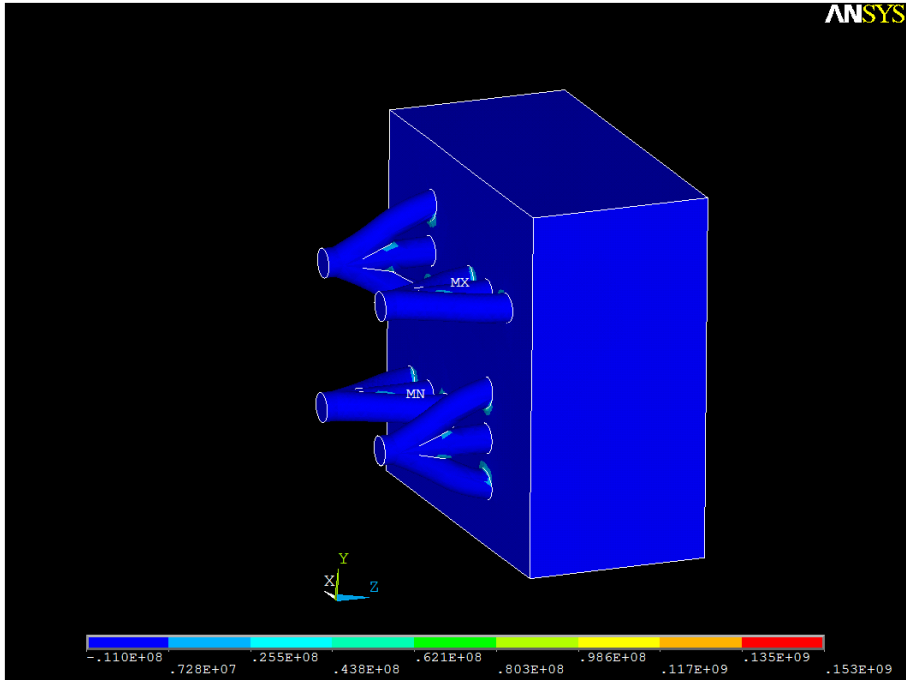
Figure 5.4: Plot of the 1st principal stresses acting in the bone portion of the interlocking strength model containing Pore Structure A under tension approaching the point of failure.
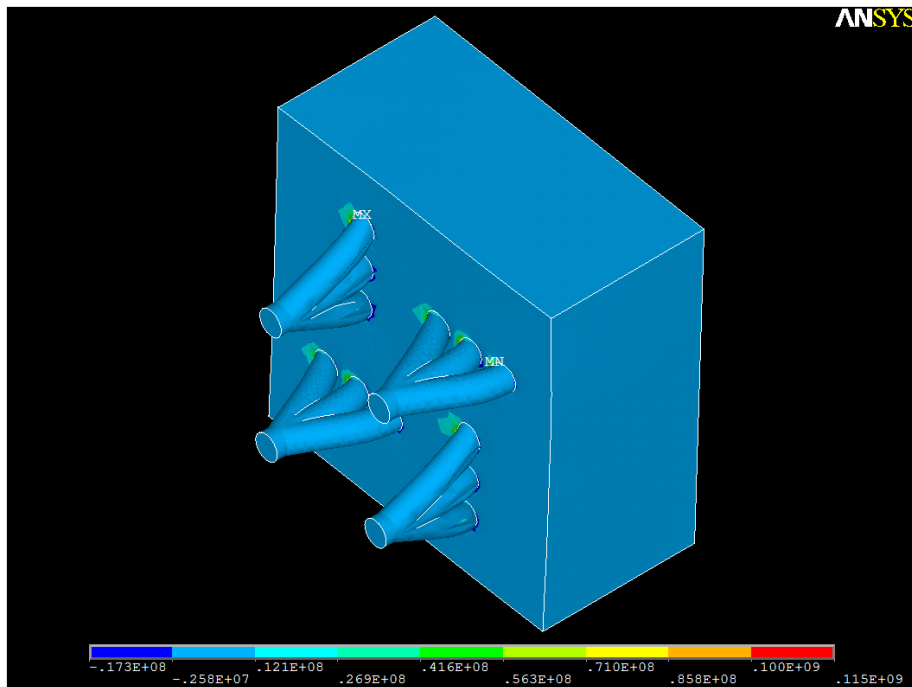
Figure 5.5: Plot of the 1st principal stresses acting in the bone portion of the interlocking strength model containing Pore Structure A under shear approaching the point of failure.
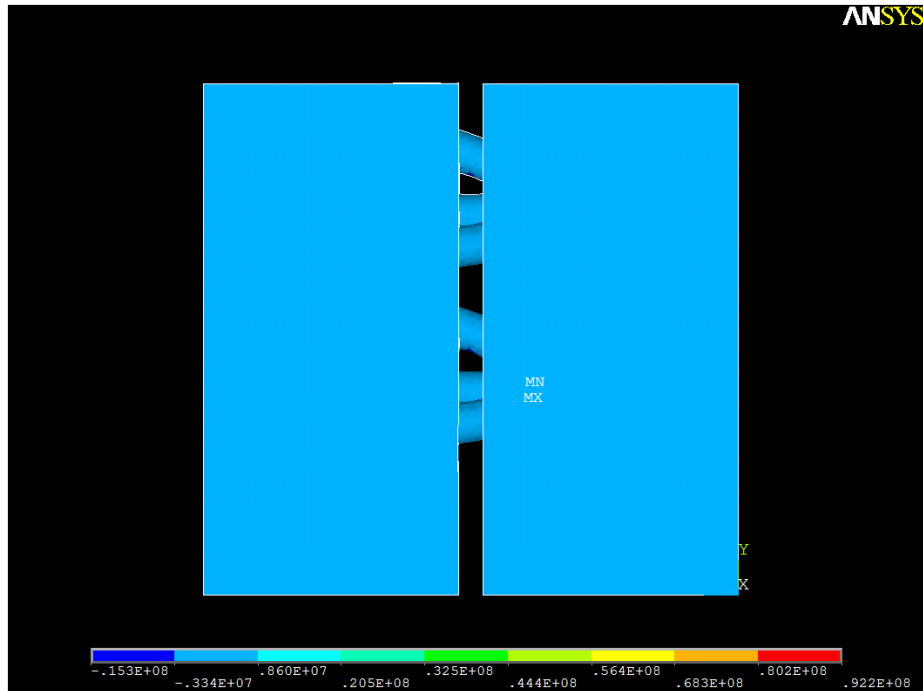
Figure 5.6: Plot of the 1st principal stresses acting in the interlocking strength model containing Pore Structure B under tension near the point of failure (with interface elements graphically suppressed). Separation at the interface is graphically exaggerated.
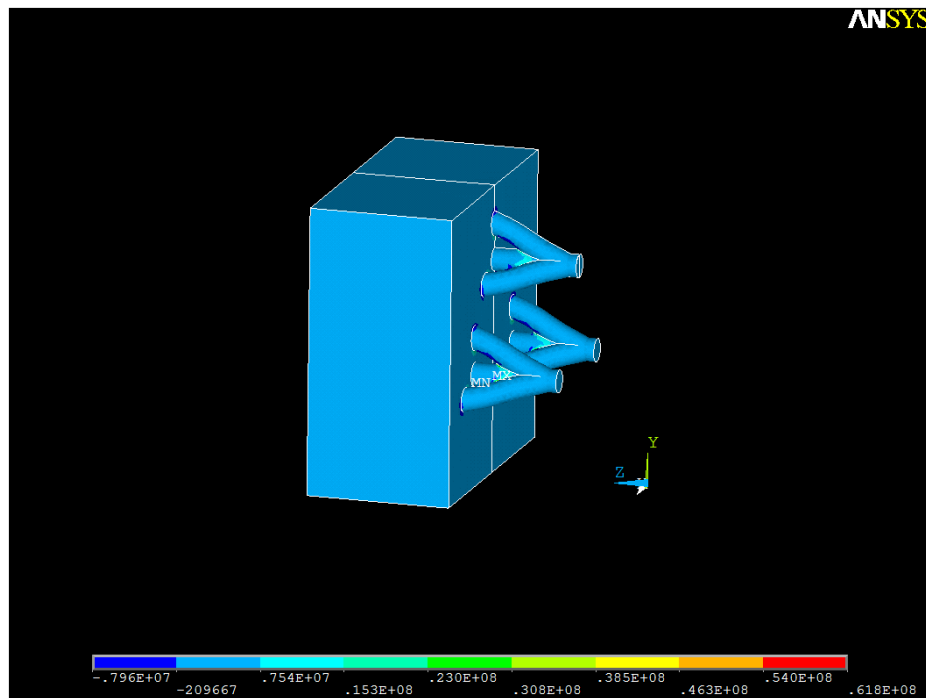
Figure 5.7: Plot of the 1st principal stresses acting in the bone portion of the interlocking strength model containing Pore Structure B when under tension approaching the point of failure.
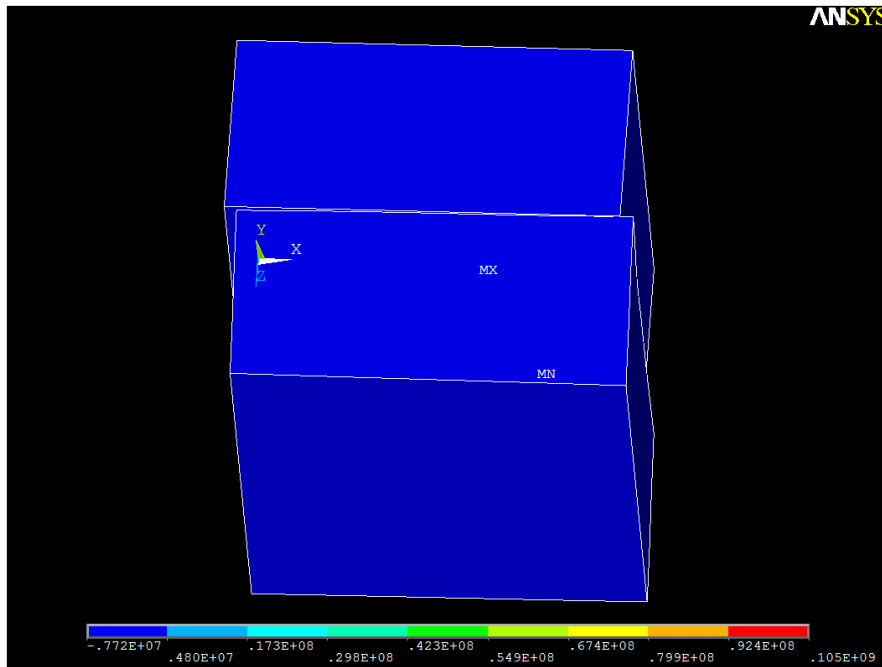
Figure 5.8: Plot of the 1st principal stresses acting in the interlocking strength model containing 12 non-intersecting pores under shear near the point of failure. Separation at the interface is graphically exaggerated.
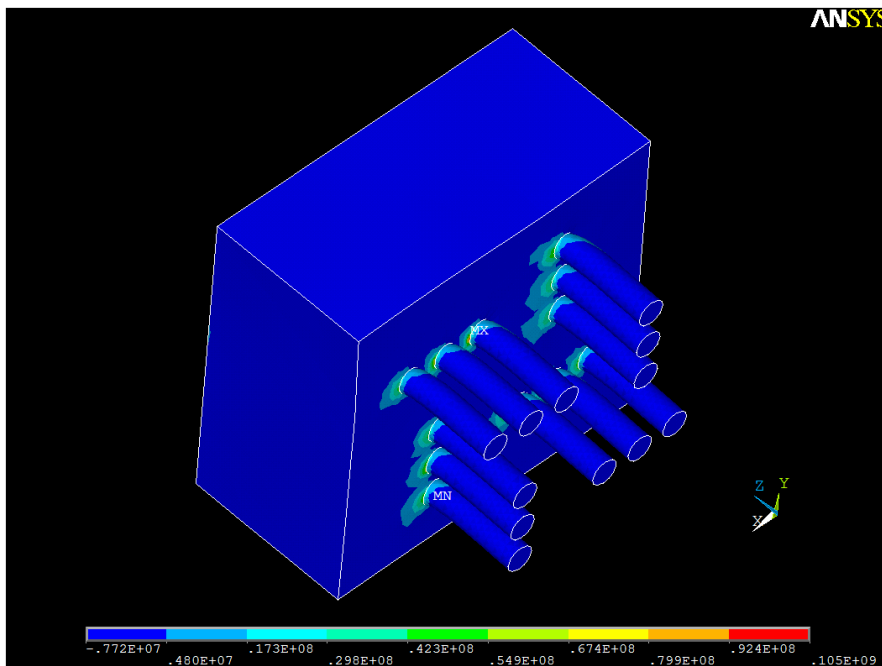
Figure 5.9: Plot of the 1st principal stresses acting in the bone portion of the interlocking strength model containing 12 non-intersecting pores when under shear approaching the point of failure.

The interlocking strengths calculated are shown in Table 5.2. Compared with a non-porous surface, the presence of even non-intersecting pores causes roughly a two-fold increase in the tensile and shear interface strength. In the case of tensile loading, this increase is due to the fact that there are now shear stresses acting at the interface (within the pores), and the strength of the interface is much higher in shear than in tension. In the case of shear loading, the increase is due to the occurrence of added mechanical interlocking.

Table 5.2: Interlocking strengths of the pore structures tested, in tension and shear. In the first two structures, where no interlocking is present, the interfacial strength is given.

Pore Structure:	No porosity	12 Non-intersecting pores	Intersecting Pore Structure A	Intersecting Pore Structure B
Tensile strength (MPa)	0.5	1	3.2	4.8
Shear strength (MPa)	4	8	5.6	8.1

In the case of the intersecting pore geometries which were considered, the increase in tensile strength at the interface compared with a non-porous interface is even more pronounced, which can of course be attributed to the major mechanical interlocking. In the case of shear, the major mechanical interlocking does not provide as clear an advantage over conventional mechanical interlocking. The shear strength in Pore Structure B is comparable to the strength in the structure of 12 non-intersecting pores. In the case of Pore Structure A, failure initiates in the bone at a noticeably lower strength compared with the case of non-intersecting pores, although the resultant strength is still somewhat higher than that seen in non-porous interfaces. This low failure strength can be attributed to the specific model setup: two of the pore clusters are aligned along

the direction of loading, and so there is a very small angle oriented parallel to the loading direction. This serves as a large stress concentrator, causing failure at a lower stress than would likely have resulted from a slightly different loading condition. More complicated models would vary the pore cluster orientation and/or loading direction to depict a more realistic implant environment. Nevertheless, an important result of this experiment is that the orientation and arrangement of pores within the "pore clusters" created at the bone/implant interface clearly impact the strength of the interface, even when the interconnectivity and pore volume are held constant among interfaces.

5.2.2 Model for Assessing Bone/Implant Interface Separation under Loading Conditions

The models used in section 5.2.1 were also utilized to qualitatively assess the susceptibility of the various simulated interfaces to wear particle intrusion. This was done by applying a small, constant tensile displacement to the models of ~0.04 microns (instead of a displacement gradually increasing until failure occurred). After this was done, a solution to the system was found, and the average stress acting in the loading direction on the front face of the bone was determined. This stress was interpreted as the average applied stress required to create the displacement imposed on the model. These applied stresses were then compared among the various models. The rationale used for this simulation was that, if a higher applied stress is required to produce a given tensile displacement in the model, then the average tensile displacement for a given applied stress (such as the stresses of daily activity) will be lower. This lower displacement equates to lower separation occurring at the bone/implant interface. Interface separation

would seem to provide an obvious mechanism for accelerated movement of wear particles into the effective joint space, and so a smaller displacement for a given stress (or, similarly, a larger stress for a given displacement) should provide better resistance to wear particle intrusion.

The results of this study are shown in Figure 5.10. It should be noted that the Y-axis scale (Applied Stress) does not extend to zero; if it did, the difference in results between each model would be barely perceptible. Nevertheless, it can be seen that the applied stress required to produce a given displacement varies slightly depending on the geometry of the model interface. A non-porous interface requires the lowest amount of applied stress for a given displacement, indicating that separation and micro-motions at the bone-implant interface will be largest for a given applied stress. The porous non-intersecting interface and porous intersecting structure "A" both require a slightly higher applied stress, and porous intersecting structure "B" requires the highest applied stress. This suggests that, in addition to having the highest interlocking strength of the models considered here, porous structure "B" will also have (slightly) better resistance to wear particle intrusion if used *in vivo*. This study also demonstrates that interface pore geometry alone can impact both the strength and cohesion of a simulated bone/implant interface, even when the amount and volume of pores is kept constant.
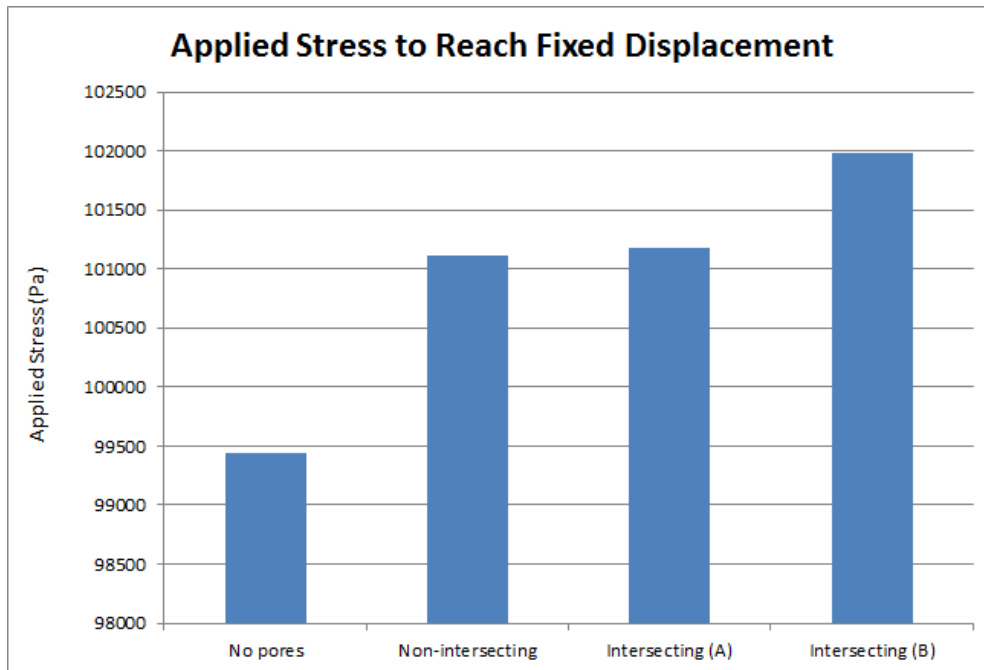
Figure 5.10: Column chart of the applied stresses required to produce a given tensile displacement within each of the interfaces considered in the interlocking strength investigation.

5.2.3 Model for Assessing Stress Shielding in Continuous vs. Discontinuous Pore Structures

While an interlocked porous interface may have a higher interfacial strength than one that is non-porous, the failure of load-bearing prosthetics is often due not to large applied loads, but to deterioration of the bone over time from lack of stimulation. Thus, it is important to assess the relative distributions of average stress between implant and bone in the case of EDM-machinable pores, to determine if an interlocked pore structure will improve reliability in this regard. With this in mind, a finite element model was created to more realistically depict operating loading conditions at the bone/implant interface. This model, while being only a rough approximation of actual implant conditions, can provide qualitative information on the amount of stimulation to the bone when different interface topographies are present.

This model sought to depict a thin cross-section of a cylindrical implant (such as a femoral stem) embedded in a bone such as the femur, which was also modeled as cylindrical. This is shown in Figure 5.11. To improve computational efficiency, a 1/8th section of the cylinder was modeled, and symmetry boundary conditions were applied such that the model's behavior would mimic that of a fully cylindrical model. The implant material was given a radius of 10mm, and the outer radius of the bone was 20mm. Both cylinder sections were modeled approximately 3.6mm thick. Three such models were created, with different structures at the interface between the bone and implant materials. The first model had a featureless (non-porous) interface. The second model contained four interlocked EDM-machinable pore structures similar to those used in Pore Structure "A" from section 5.2.1 but with an angle of inclination of 32° instead of 25°. Two of these structures were embedded within the 1/8th-symmetry model, and two were divided in half and positioned at the extreme edges of the symmetric model, as seen in Figure 5.12. The third model contained 12 perpendicularly-cut (non-intersecting) pores, also seen in Figure 5.12. The positions of pores were similar between the second and third models, and the volume occupied by the pores was made equal in both cases. The meshing procedures from the models described above were applied to this model as well. The Cohesive Zone interface properties applied to the interlocking strength models were also applied to these models, to more closely approximate real implant behavior.
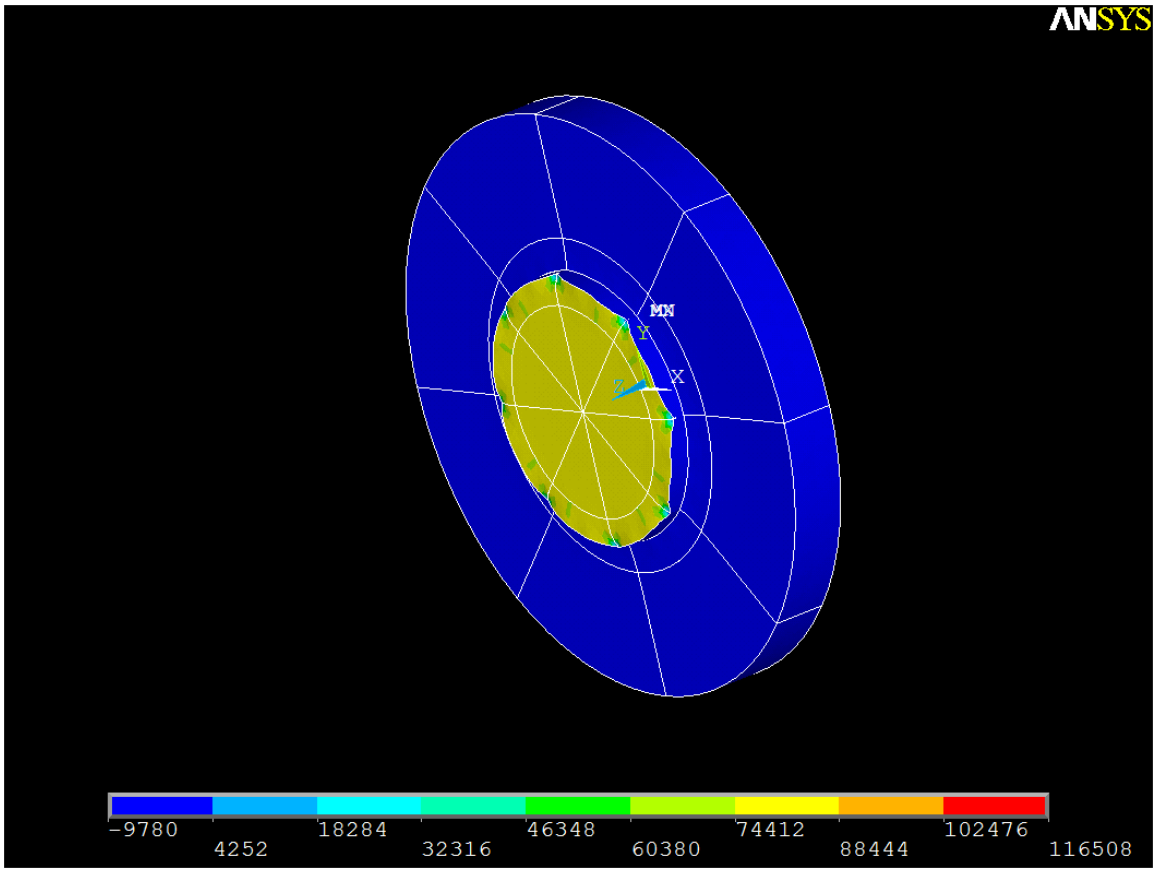
Figure 5.11: Symmetry expansion of the model simulating a cylindrical implant centered within a cylindrical bone. In the above image, tension was applied to the implant (yellow region) along the cylindrical axis.
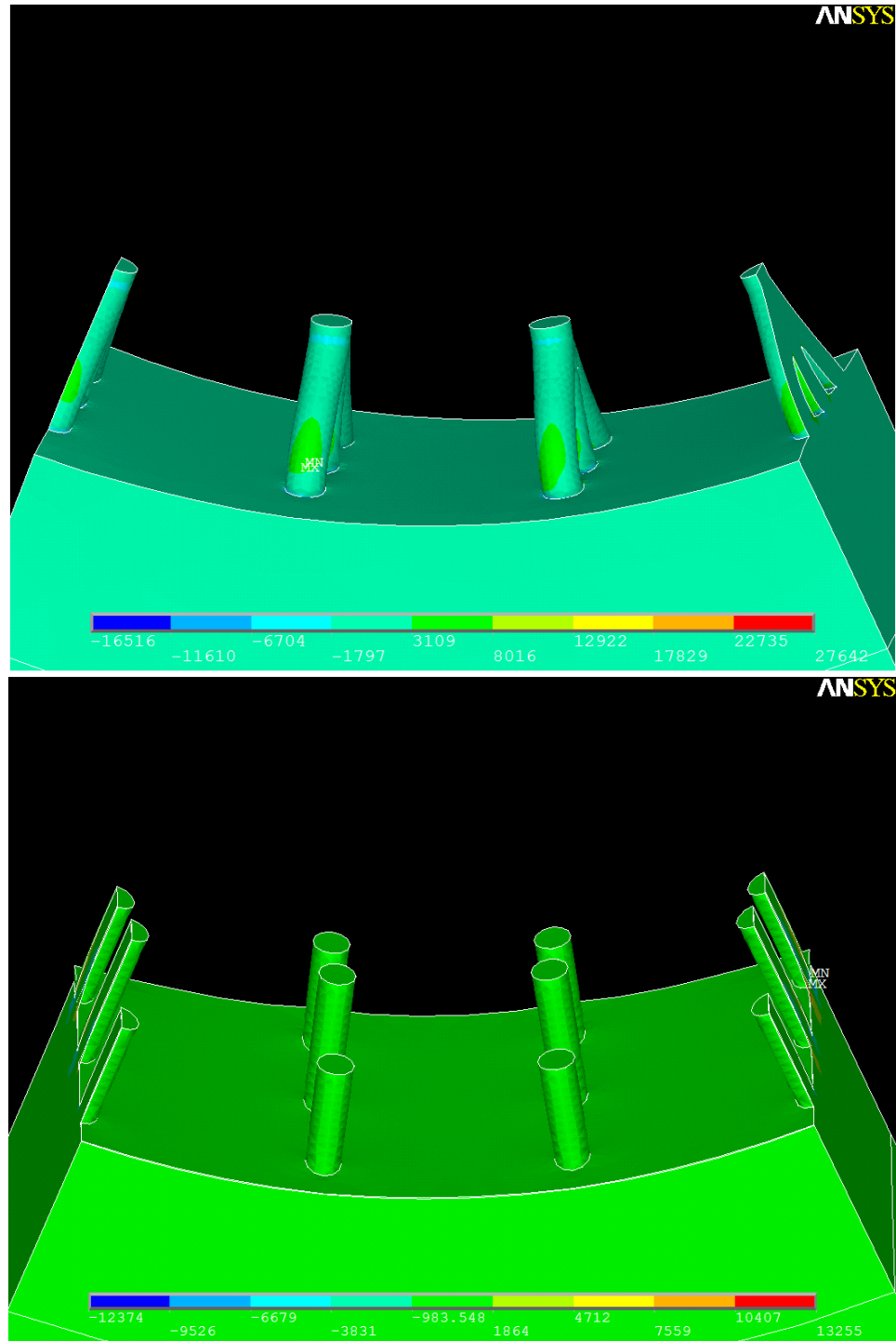
Figure 5.12: Illustration of the pore arrangement for the stress shielding analysis in the simulated bone material, (top) in the case of interconnected pores and (bottom) in the case of non-interconnected pores.

Two implant loading conditions were considered for these models: tensile and compressive stresses acting on the implant material along its cylindrical axis. To apply this loading, uniform pressure of 75kPa was applied to the front face of the implant material (the yellow region of Figure 5.11). The entire back face of the model, including implant and bone materials, was constrained against moving along the direction of loading. After these constraints were applied, a solution to the system was found, and the average von Mises and hydrostatic stresses in the bone and implant were calculated. Only the portions of the model within 2mm on either side of the bone/implant interface were analyzed, as this region contained the vast majority of differences in stress between each model. This simplified study sought to qualitatively assess the relative differences between each model, so examining only the portion of the model near the interface simplified this assessment. Example images of the models after loading are shown in Figures 5.13 through 5.16.
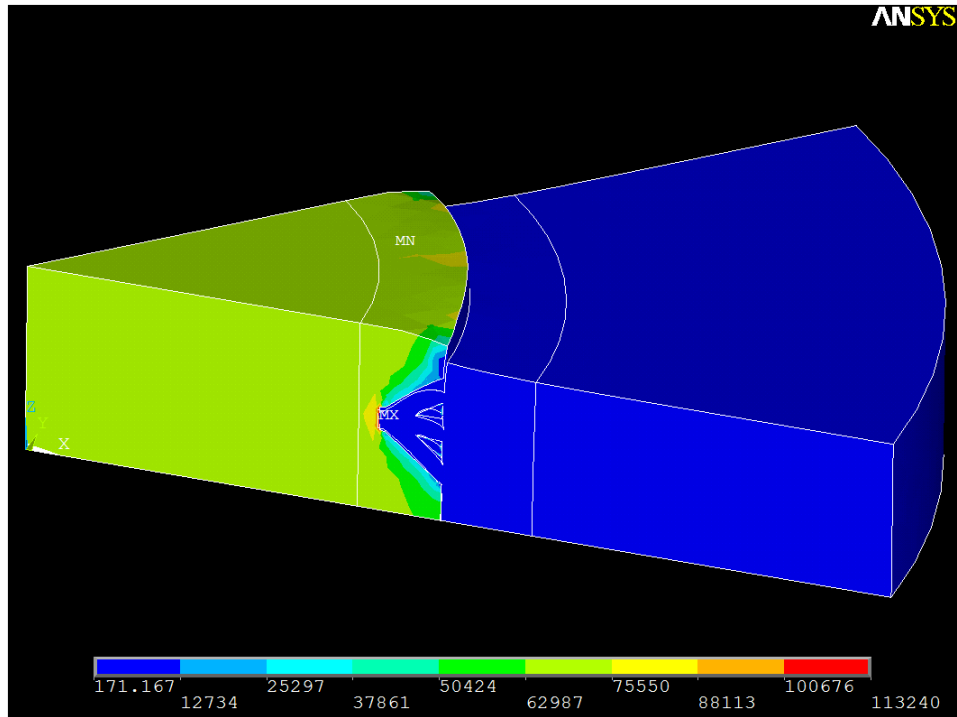
Figure 5.13: Stress distribution model for the case of interconnected pores. This graph shows von Mises stresses acting on the model when tension was applied.
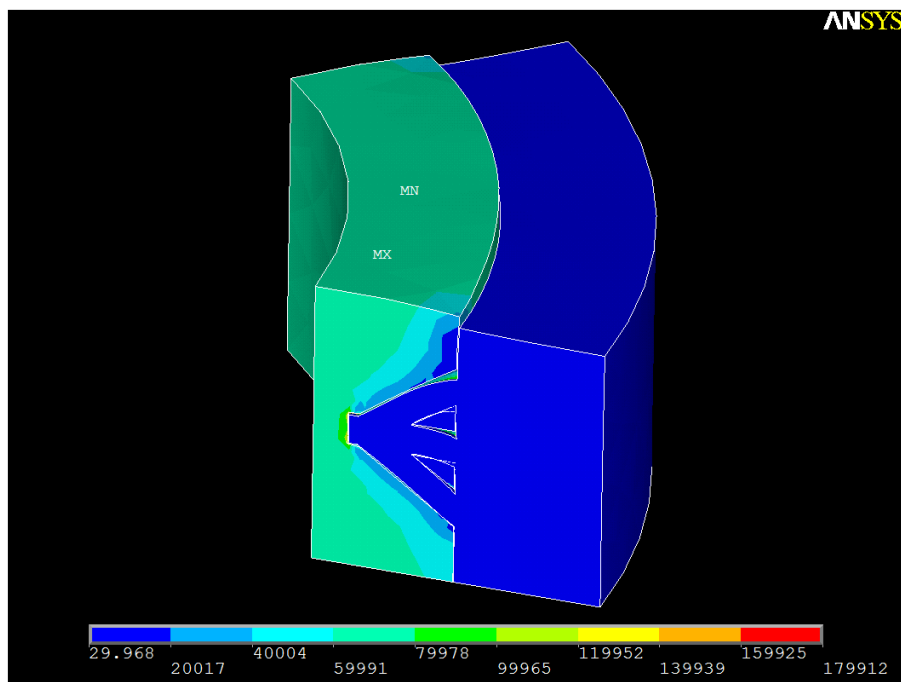
Figure 5.14: Stress distribution model for the case of interconnected pores. This graph shows von Mises stresses acting in the portion of the model from which stress distribution information was extracted.
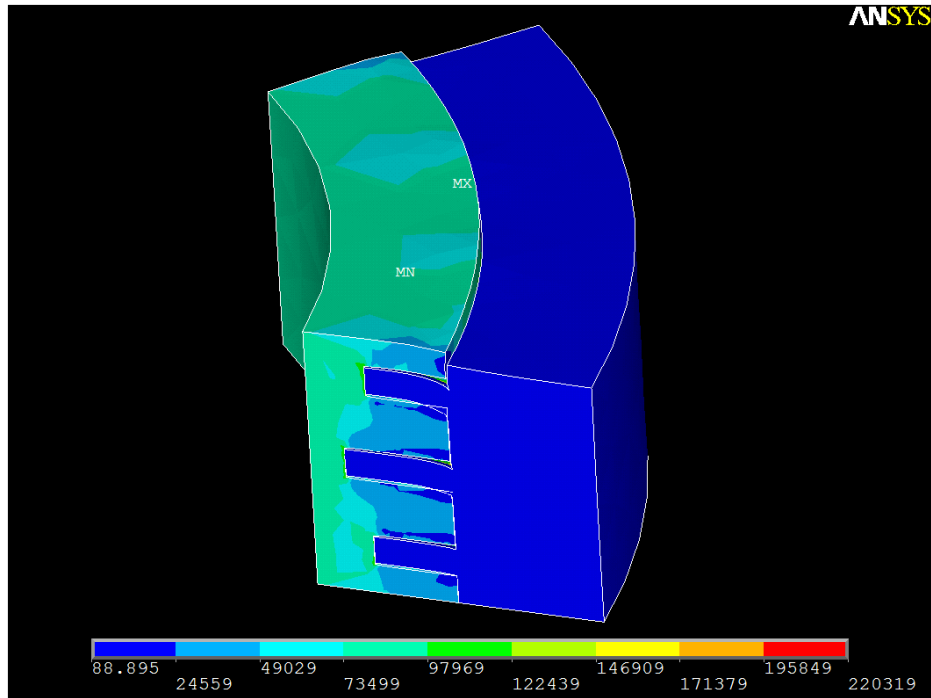
Figure 5.15: Stress distribution model for the case of non-interconnected pores. This graph shows von Mises stresses acting in the portion of the model from which stress distribution information was extracted.
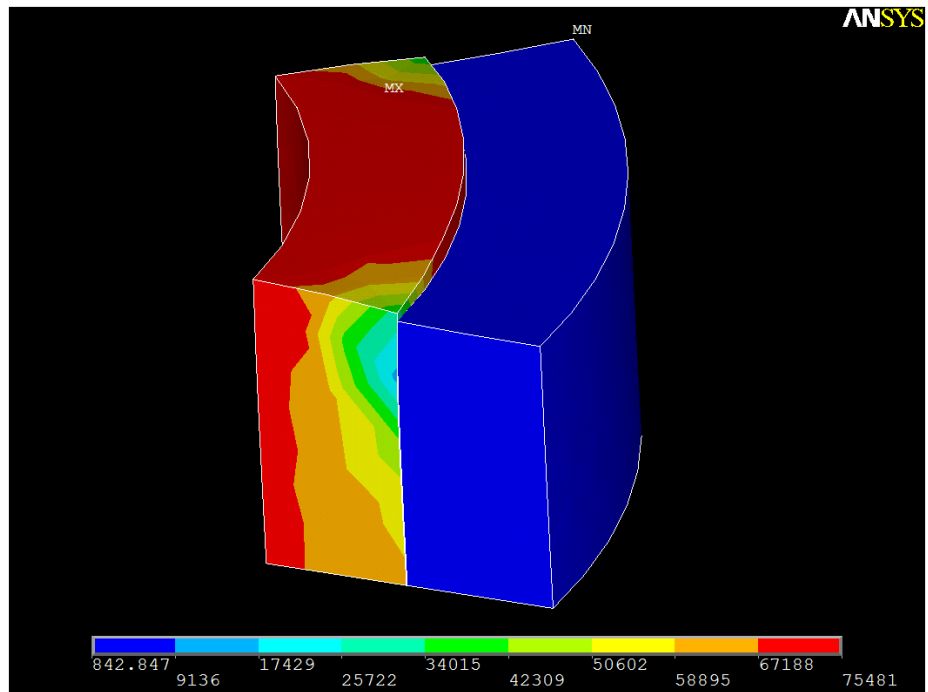
Figure 5.16: Stress distribution model for the case of no porosity. This graph shows von Mises stresses acting in the portion of the model from which stress distribution information was extracted.

The results of this study are shown in Figure 5.17. It can be seen that in both measures of average stress, the values for both types of porous interface greatly exceed the values for the non-porous interface. More interestingly, though, the stress ratios acting in the interconnected porosity are higher than in the non-interconnected case, despite having an equal volume and similar arrangement on the interface. The ratios observed were virtually identical in tensile and compressive loading.

In order to minimize stress shielding, the implant should transfer as much of operating stresses to the bone as possible (i.e. the ratio of stress in the bone to stress in the implant should approach unity). Therefore, it can be inferred that pores with EDM-machinable geometries will do a better job of preventing stress shielding in the bone when interconnected structures are present at the interface.
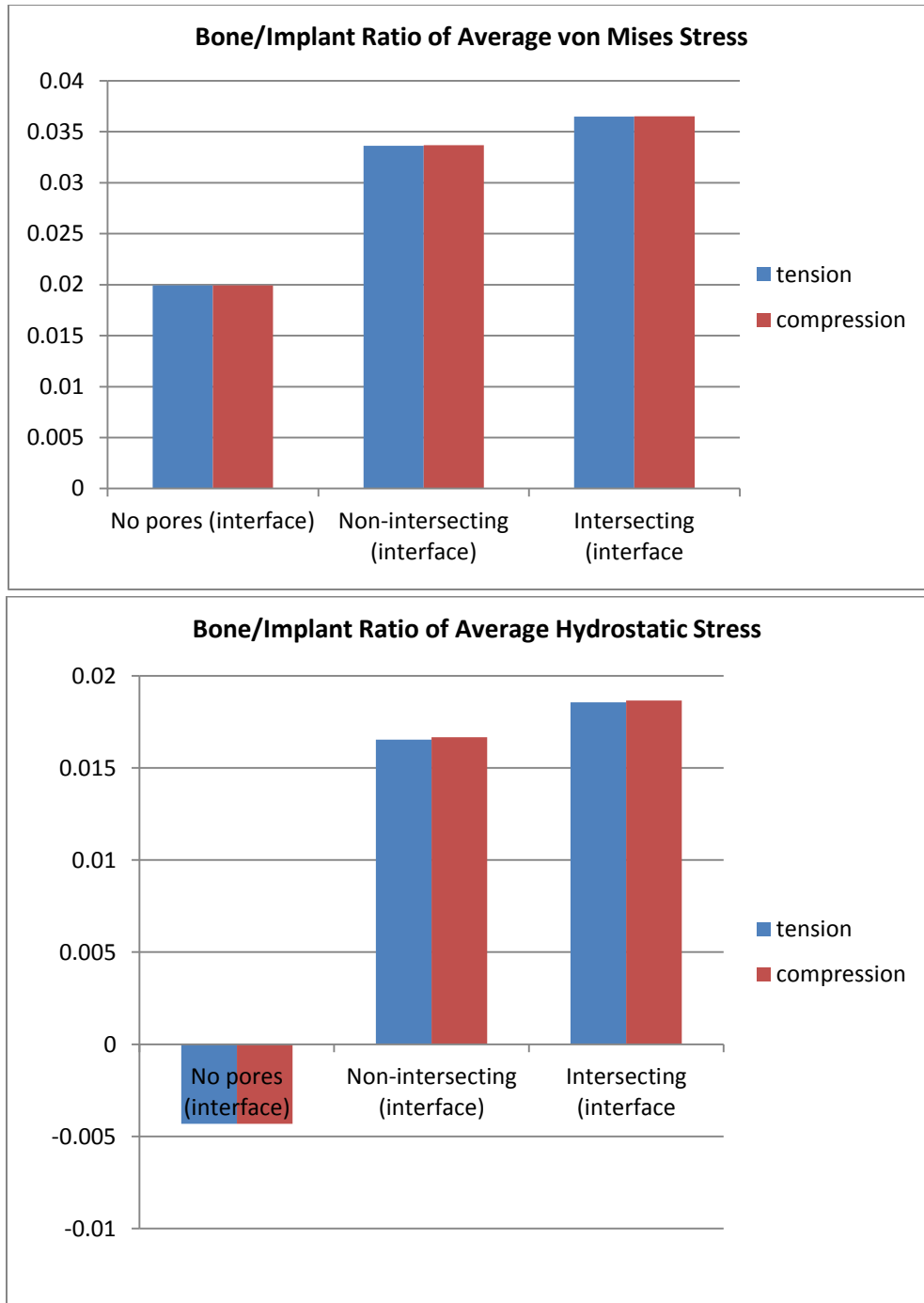
Figure 5.17: Comparison of the bone/implant ratios of (top) von Mises and (bottom) hydrostatic stresses acting near the interface for the three stress shielding models tested.

5.3 Conclusions

A three-dimensional finite element modeling (FEM) study was done on the impact of EDM-machinable porous structures on the mechanical properties of the interface between titanium and cortical bone. Two pore structures were selected, based on preliminary work and computational efficiency, for determination of their interlocking strength. It was found that the interlocking strength of both structures was far higher than the interfacial strength of a non-porous interface, and greater than or comparable to the strength of a porous, non-interconnected interface depending on whether tensile or shear loading was applied. In addition, it was found that the pore clusters had significantly different interlocking strengths despite having equal volumes, amounts of interconnectivity, and angles of inclination, suggesting that pore orientation has a significant impact on interface strength.

The relation between applied stress and interface separation in the above-mentioned models was also studied. It was found that a higher applied stress was required to produce the same amount of tensile displacement in the models containing interlocked porous interfaces compared with non-porous and non-interlocked interfaces. This suggests that the interlocked interfaces will be (slightly) less susceptible to wear particle intrusion. In addition, the amount of applied stress varied between the two interlocked models, again indicating that interface geometry impacts the cohesion of the interface under otherwise similar conditions.

Finally, the average von Mises and hydrostatic stress distributions in a simple mock implant model were determined when non-porous, porous-interconnected and porous-non-interconnected interfaces are present. The average bone/implant stress ratio

was highest in the interconnected interface, suggesting that this interface will be the most resistant to stress shielding over time.

Chapter 6

Conclusions

This investigation sought to provide a preliminary understanding of the reliability of a recently-developed implant technology (surface modification of load-bearing prosthetics through machining of sub-surface-continuous pores by EDM) from a biological and mechanical perspective. Specifically, it addressed four issues: the survivability and activity of bone-forming cells within the surface modification, the strength of the interface formed under static loads, the susceptibility of the interface to separation-assisted wear particle intrusion, and the resultant stress shielding (i.e. the ratio of average stress acting in the bone to the average stress acting in the implant) which occurs. A combination of biomaterials strategies, microscopy, characterization, and finite element modeling were utilized to address these issues. The investigation yielded the following results:

1. To verify the survivability and mineralization potential of cells within deep pores in titanium fabricated using the EDM technique, seeding and differentiation of bovine mesenchymal stem cells was performed on Grade 4 titanium disks containing non-intersecting EDM-prepared pores over a period of 12 weeks. The proliferation and mineralization of the stems cells was characterized using fluorescence microscopy, SEM, EDS, and confocal microscopy. Although a small sample size of disks was available for testing, some of the disks exhibited large amounts of cell proliferation and mineralization. Specifically, after 12 weeks of cell growth, disks with a variety of properties (e.g. surfaces of

environmentally-oxidized and intentionally-oxidized titanium, pores terminating within the disk as well as through-cut pores) demonstrated mineralized matrix in ~88% of their pores. The ratio of calcium to phosphorus within this mineralized matrix approached the ratio found in healthy bone, indicating extensive mineralization in the matrix. In many cases, the matrix extended to the full depth of the pore in which it was found, suggesting that *in vivo* bone growth could extend into deeper interconnected pore structures. Although all samples in this study received the same treatments at the same time, other disks were found to have virtually no mineralization. It is likely that the stem cells seeded onto these disks died and/or de-adhered from the samples before they could produce mineralization, although the reason for this is unclear. The reason is expected to be anomalous, such that a larger percentage of samples would exhibit mineralization given a larger sample size.

2. A three-dimensional finite element model was developed to assess the interlocking strength of various interfaces achievable using the EDM method. Two pore structures were selected, based on preliminary studies and computational efficiency, and were subjected to simulated tensile and shear loading until failure occurred. The interlocking strength of both structures exceeded or was comparable to the interfacial strength of other porous and non-porous interfaces, and depends on the orientation of the interlocked pores under otherwise equal conditions.

3. Additional finite element studies were done on the above-mentioned pore structures, to assess the susceptibility of various interfaces to wear particle

intrusion under loading. It was found that the applied stress required to produce a given tensile displacement in the model varied somewhat based on the interconnectivity of the interface; interlocked structures required a higher applied stress to reach a given displacement compared with non-interlocked interfaces, suggesting bear particle intrusion resistance. In addition, interface geometry impacted the interface separation under otherwise equal conditions, as was observed in Conclusion 2.

4. A simple finite element study was performed regarding the effect of EDM-produced pore interconnectivity on the stress shielding resistance of a mock implant. It was found that under equal loading conditions and equal conditions of pore number, position, and volume, an interconnected EDM-machinable pore structure will transfer stress from implant to bone more effectively than a discontinuous pore structure, suggesting better stress shielding resistance. Both structures exhibited substantially better stress transfer than a non-porous interface.

Chapter 7

Suggestions for Future Work

1. Continued *in vitro* characterization of cell activity within EDM-prepared pore structures, especially interconnected structures. Funding for this work limited the number and complexity of physical samples which could be prepared, and so the full behavior of bone-forming osteoblasts within EDM-prepared interconnected pores was not verified. However, literature on other surface processes suggests that pore interconnectivity should not adversely affect cell activity.

2. Determination of interlocking strength and stress distribution in more complex pore geometries using FEM.

3. FEM studies incorporating the effects of TiO_2, hydroxyapatite, or other coatings and surface preparations which can be used in tandem with the EDM method. These coatings affect the interface strength of the bone (and have their own mechanical properties which are different from bone's and titanium's as well), and so may have an impact on the interlocking strength of the implant.

4. *In vitro* characterization of cell activity within EDM-prepared pore structures which have the above-mentioned additional treatments/coatings.

5. *In vivo* studies to examine the actual osseointegration of EDM-prepared porous implants in the body. A combination of hard-tissue histology and mechanical testing would determine the bone/implant contact area and mechanical strength of the implant compared with implants prepared using traditional methods.

Appendix A

Procedures Used for Model Development in ANSYS

The following commands were utilized in the ANSYS 11.0 FEM program to build and test the various structures described in this work. The "Procedure Used for Creation of Model for Interlocking Strength Analysis" provides all steps needed to create one of the models examined in this work, although the instructions for creating the pore clusters have been generalized to describe only the creation of a single pore cluster at the center of the model. Creation of more complicated pore structures requires the same basic steps, the only difference being that the X and Y coordinates of the Working Plane should be varied by the user based on the intended pore structure geometry. Creation of the stress shielding model involves the creation of different geometries through the CAD interface, and differences in the boundary conditions and stresses/displacements applied to the model. However, all the necessary information needed to understand the ANSYS interface and build a specific model is included here.

Simulations were performed using a combination of graphical user interface (GUI) commands and the ANSYS Parametric Design Language (APDL) when the desired features were inaccessible through the GUI. GUI commands were issued through the ANSYS Main Menu or Utility Menu (items 1 and 3 in Figure A.1) and APDL commands were issued in the APDL Command Line (item 2 in Figure A.1).
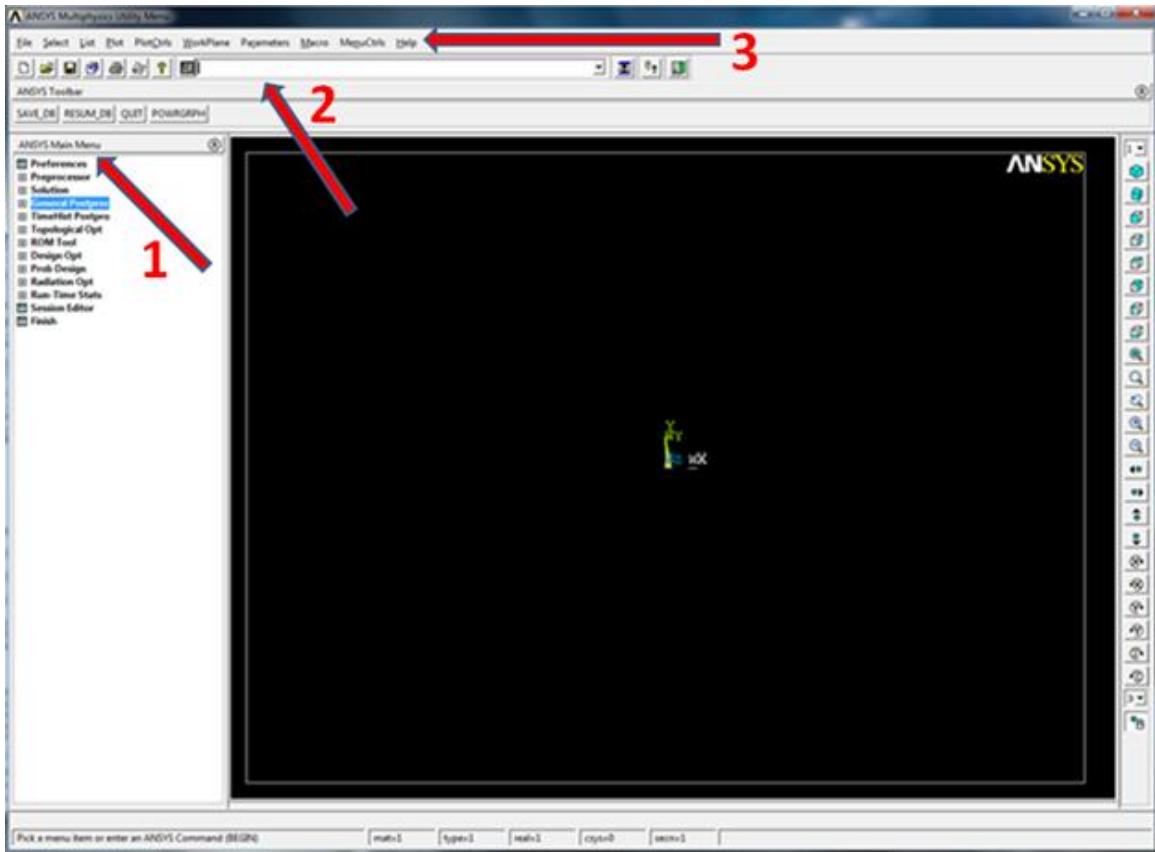
Figure A.1: Screenshot of the ANSYS interface, with arrows indicating (1) the ANSYS Main Menu, (2) the APDL Command Line, and (3) the Utility Menu used to create and analyze models.

Procedure Used for Creation of Model for Interlocking Strength

Analysis

- **Main Menu>Preferences>Structural**. This ensures that only structural changes are made to the model for this experiment, so that thermal, electromagnetic, or other changes are not made accidentally.

- **Main Menu>Preprocessor>Element Type>Add/Edit/Delete>Add>Solid187**. SOLID187 is a 3-dimensional, quadratic, 10-node tetrahedral element well suited

for models with complex shapes. Quadratic elements produce more accurate results than linear elements at the cost of additional calculation time.

- **Main Menu>Preprocessor>Element Type>Add/Edit/Delete>Add>Inter204**. INTER204 is a 3-dimensional Cohesive Zone element used in ANSYS for simulating the delamination of interfaces in composite materials.

- **Command Line>NROPT,FULL,,,ON**. This command must be issued during the "Preprocessor" phase of model creation. This command activates the Newton-Raphson option, which is an iterative process used in finding the solution to nonlinear analyses.

- **Main Menu>Preprocessor>Material Props>Material Models>Structural> Linear> Elastic>Isotropic**. The first material to be simulated in these models is Grade 4 commercially pure (CP) titanium, which has a Young's modulus of 105 GPa. The Poisson's ratio of the material was assumed to be 0.3, which is commonly done in FEM simulations of this type.

- **Main Menu>Preprocessor>Material Props>Material Models>Structural> Linear> Elastic>Isotropic**. The second material to be simulated in these models is bulk cortical bone, which has a Young's modulus of ~6.8 GPa according to Tarala et al. The Poisson's ratio of the material was assumed to be 0.3, which is commonly done in FEM simulations of this type.

- **Command Line>TB,CZM,3,,,EXPOTBDATA,1,0.3E6,0.1,1.** This command should be issued during the "Preprocessor" phase of model creation. This command defines material #3 as an exponential Cohesive Zone material (once materials 1 and 2 have already been defined using the methods described above).

Based on the input values relating to maximum tensile stress, maximum tensile displacement, and maximum shear stress, the Young's modulus of this material will exponentially decrease as its deformation increases. ANSYS uses this process to approximate the failure of the interface between materials while maintaining numerical convergence of the model.

- **Main Menu>Preprocessor>Modeling>Create>Volumes>Block>By Dimensions.** The dimensions of the titanium model to be considered (5000 units in the X direction by 5000 units in the Y direction by 2500 unites in the Z direction) are input here.

- **Utility Menu>WorkPlane>Offset WP to>XYZ locations.** The working plane was used to create the pore structure, which required moving the working plane to the origin of the pore within the model (coordinates of X=2500, Y=2500, Z=1000).

- **Main Menu>Preprocessor>Modeling>Create>Volumes>Cylinder>By Dimensions.** Pores were given an outer radius of 200 and were extruded from 0 to 3000 in the Z direction.

- **Utility Menu>WorkPlane>Offset WP to>XYZ locations.** To maintain a constant, flat geometry at the bottom of each pore cluster, the bottom of each angular pore was made to intersect the perpendicular pore at X=2500, Y=2500, and Z=1200.

- **Utility Menu>WorkPlane>Offset WP by increments…** The working plane was tilted in the X, Y, and Z directions by specific amounts to create the desired angle between the perpendicular pore and the working plane Z axis.

- **Main Menu>Preprocessor>Modeling>Create>Volumes>Cylinder>By Dimensions.** This step and the previous one were repeated until the desired pore geometry was made.

- **Main Menu>Preprocessor>Modeling>Operate>Booleans>Add> Volumes.** Manually select all pores to merge them into a single entity.

- **Main Menu>Preprocessor>Modeling>Operate>Booleans>Partition> Volumes.** Select the pore structure and the surrounding block to partition them into two separate entites.

- **Main Menu>Preprocessor>Modeling>Delete>Volumes and Below.** Select all of the pieces of the pore structure which protrude from the surrounding block, and delete them.

- **Utility Menu>WorkPlane>Align WP with>Global Cartesian.**

- **Main Menu>Preprocessor>Modeling>Create>Volumes>Block>By Dimensions.** Create the block of bone material, with coordinates of $X = 0$ to 5000, $Y = 0$ to 5000, and $Z = 2500$ to 5000. Add this block to the pore structure material using the Add function.

- **Main Menu>Preprocessor>Modeling>Operate>Booleans>Glue> Volumes.** Glue all volumes together.

- **Main Menu>Preprocessor>Meshing>Mesh Attributes>Picked Volumes.** Assign material #1 to the titanium block, and material #2 to the bone block.

- **Main Menu>Preprocessor>Meshing>MeshTool.** Select a SmartSize value of 4 and mesh all volumes. If meshing is unsuccessful for the specific model, try again with a finer mesh value (i.e. 3 or smaller).

- **Utility Menu>Select>Component Manager.** This function should be used after the model has been meshed. The Component Manager defines "components" within the model, which can be used to define interface elements between two components. Once the above path has been followed, the "Create Component" button may be pressed. By choosing the desired volumes in the model, a component can be defined. This investigation called for defining two components (the titanium component and the bone component), called CM_1 and CM_2 by the program.

- **Command Line>type,2>mat,3>czmesh,CM_1,CM_2.** This command should be issued during the "Meshing" phase of model creation, after components CM_1 and CM_2 have been defined. This command defines Cohesive Zone elements of element type #2 (INTER204 for this investigation) and material #3 (the cohesive zone material) between components CM_1 and CM_2.

- **Main Menu>Preprocessor>Coupling/Ceqn>Couple DOFs.** Select all nodes on the front face of the bone material. Assign them coupling set #1, and define the constraint along the Z direction.

- **Main Menu>Solution>Define Loads>Apply>Structural>Displacement>On Areas.** Select the front face of the bone material, and apply a displacement along the Z direction (for tension) or the X direction (for shear). To improve convergence of the models, it is recommended that the first applied displacement be very small (~0.04 micrometers), and then the displacement can be gradually increased on successive iterations of the model.

- **Main Menu>Solution>Define Loads>Apply>Structural>Displacement>On Areas.** Select the back face of the titanium material, and set the displacement in all directions equal to zero.

- **Main Menu>Solution>Solve>Current LS.** Press OK to solve the system.

Appendix B

Problems Encountered During Finite Element Model Preparation, and

Solutions Devised

Modeling material failure such as interface delamination is a highly non-linear process in which large abrupt changes can occur in the model geometry. Consequently, simulating this process is very susceptible to solution trouble due to numerical non-convergence. The process available in ANSYS which was used in this investigation to model interface failure is the Exponential Cohesive Zone Model (CZM) technique. This technique attempts to avoid numerical instability in the model by causing less abrupt failure at the interface. Based on user-inputted values, the mechanical properties of the interface vary exponentially as a function of separation at the interface. The stress supported by the interface as a function of applied displacement increases in the expected manner up to a point determined by user input. Above this point, the stress supported at the interface smoothly transitions into an exponential decay function, such that the interface has exponentially decreasing cohesion. Although this CZM technique improves solubility of a model, it makes the precise moment of interface failure difficult to identify. In addition, solubility and accuracy of the model still depend strongly on the user-inputted values for CZM, model mesh density, loading conditions, and boundary conditions. Considerable effort was expended identifying conditions which approximate the tensile and shear behavior of the bone/implant interface yet also produce stable solutions for a variety of model geometries. Suggestions for effective application of the CZM method are described here.

In general, finer mesh densities will yield better CZM results, at the obvious expense of computation time. It was also found that applying the intended displacement to the model gradually, starting at very small displacements and gradually increasing the displacement each time a solution is found, tends to improve chances of convergence. Applying boundary conditions which were not required in the absence of a CZM interface may also be necessary. For example, in certain models, presently-unexplained rotation and translation were observed to occur at the interface where no such distortions occurred in CZM-free models of the same geometry. Additional boundary conditions could usually be found which were physically sensible and prevented this phenomenon (for example, restricting the degrees of freedom along an axis of symmetry in the model prevented unwanted rotation). Ultimately, though, trial-and-error variation of the user-inputted parameters was needed to achieve satisfactory model behavior. It was empirically found that input values of $C1 = 300000$, $C2 = 0.1$, and $C3 = 1$ produced interface behavior which reasonably approximated the tensile and shear strengths of the bone/implant interface.

References

1. Geetha, M., Singh, A.K., Asokamani, R., Gogia, A.K., *Ti based biomaterials, the ultimate choice for orthopaedic implants - A review.* Progress in Materials Science, 2009. **54**(3): p. 397-425.

2. Rack, H.J., Qazi, J. I., *Titanium alloys for biomedical applications.* Materials Science & Engineering C-Biomimetic and Supramolecular Systems, 2006. **26**(8): p. 1269-1277.

3. Long, M., Rack, H.J., *Titanium alloys in total joint replacement - a materials science perspective.* Biomaterials, 1998. **19**(18): p. 1621-1639.

4. Wang, K., *The use of titanium for medical applications in the USA.* Materials Science and Engineering a-Structural Materials Properties Microstructure and Processing, 1996. **213**(1-2): p. 134-137.

5. Liu, X.Y., Chu, P.K., Ding, C.X., *Surface modification of titanium, titanium alloys, and related materials for biomedical applications.* Materials Science & Engineering R-Reports, 2004. **47**(3-4): p. 49-121.

6. Cachinho, S.C.P., Correia, R.N., *Titanium scaffolds for osteointegration: mechanical, in vitro and corrosion behaviour.* Journal of Materials Science-Materials in Medicine, 2008. **19**(1): p. 451-457.

7. Ryan, G., Pandit, A., Apatsidis, D.P., *Fabrication methods of porous metals for use in orthopaedic applications.* Biomaterials, 2006. **27**(13): p. 2651-2670.

8. Lopez-Heredia, M.A., Goyenvalle, E., Aguado, E., Pilet, P., Leroux, C., Dorget, M., Weiss, P., Layrolle, P., *Bone growth in rapid prototyped porous titanium implants.* Journal of Biomedical Materials Research Part A, 2008. **85A**(3): p. 664-673.

9. Lopez-Heredia, M.A., Sohier, J., Gaillard, C., Quillard, S., Dorget, M., Layrolle, P., *Rapid prototyped porous titanium coated with calcium phosphate as a scaffold for bone tissue engineering.* Biomaterials, 2008. **29**(17): p. 2608-2615.

10. Bae, S.E., Park, K., Han, D.K., *Characteristics and Cell Adhesion on Hydroxyapatite-Formed Titanium by Surface Modification.* Tissue Engineering and Regenerative Medicine, 2011. **8**(4): p. 116-122.

11. An, S.W., Thompson, A.D., Betz, M.W., Caccamese, J.F., Coletti, D.P., Sauk, J.J., Fisher, J.P. *Scaffold facilitated osteoblastic differentiation for orbital bone repair*. in *Annual Biomedical Engineering Society Meeting*. 2005.

12. Kim, K., Fisher, J.P., *Nanoparticle technology in bone tissue engineering.* Journal of Drug Targeting, 2007. **15**(4): p. 241-252.

13.   Spoerke, E.D., Murray, N.G., Li, H.L., Brinson, L.C., Dunand, D.C., Stupp, S.I., *A bioactive titanium foam scaffold for bone repair.* Acta Biomaterialia, 2005. **1**(5): p. 523-533.

14.   Torres, Y., Pavon, J.J., Nieto, I., Rodriguez, J.A., *Conventional Powder Metallurgy Process and Characterization of Porous Titanium for Biomedical Applications.* Metallurgical and Materials Transactions b-Process Metallurgy and Materials Processing, 2011. **42**(4): p. 891-900.

15.   Yang, B.C., Uchida, M., Kim, H.M., Zhang, X.D., Kokubo, T., *Preparation of bioactive titanium metal via anodic oxidation treatment.* Biomaterials, 2004. **25**(6): p. 1003-1010.

16.   Calderon, J.H., Valencia, R.M., Casassa, A.A., Sanchez, M.A., Espinosa, R., Ceja, I., *Biomechanical Anchorage Evaluation of Mini-Implants Treated With Sandblasting and Acid Etching in Orthodontics.* Implant Dentistry, 2011. **20**(4): p. 273-279.

17.   Riedel, N.A., Williams, J.D., Popat, K.C., *Ion beam etching titanium for enhanced osteoblast response.* Journal of Materials Science, 2011. **46**(18): p. 6087-6095.

18.   Tuncer, N., Arslan, G., Maire, E., Salvo, L., *Influence of cell aspect ratio on architecture and compressive strength of titanium foams.* Materials Science and Engineering a- Structural Materials Properties Microstructure and Processing, 2011. **528**(24): p. 7368-7374.

19.   Murr, L.E., Amato, K.N., Li, S.J., Tian, Y.X., Cheng, X.Y., Gaytan, S.M., Martinez, E., Shindo, P.W., Medina, F., Wcker, R.B., *Microstructure and mechanical properties of open-cellular biomaterials prototypes for total knee replacement implants fabricated by electron beam melting.* Journal of Mechanical Behavior of Biomedical Materials, 2011. **4**(7): p. 1396-1411.

20.   Baas, J., Svaneby, D., Jensen, T.B., Elmergaard, B., Bechtold, J., Soballe, K., *Coralline hydroxyapatite granules inferior to morselized allograft around uncemented porous Ti implants: Unchanged fixation by addition of concentrated autologous bone marrow aspirate.* Journal of Biomedical Materials Research Part A, 2011. **99A**(1): p. 9-15.

21.   Saidpour, S.H., *Assessment of carbon fibre composite fracture fixation plate using finite element analysis.* Annals of Biomedical Engineering, 2006. **34**(7): p. 1157-1163.

22.   Rüger, M., Gensior, T., Herren, C., von Walter, M., Ocklenburg, C., Marx, R., Erli, H., *The removal of Al2O3 particles from grit-blasted titanium implant surfaces: Effects on biocompatibility, osseointegrations and interface strength in vivo.* Acta Biomaterialia, 2010. **6**(7): p. 2852-2861.

23. Alzubaydi, T.L., AlAmeer, S.S., Ismaeel, T., AlHijazi, A.Y., Geetha, M., *In vivo studies of the ceramic coated titanium alloy for enhanced osseointegration in dental applications.* Journal of Materials Science-Materials in Medicine, 2009. **20**: p. 35-42.

24. Probster, L., Voigt, C., Fuhrmann, G., Gross, U.M., *Tensile and torsional shear-strength of the bone implant interface of titanium implants in the rabbit.* Journal of Materials Science-Materials in Medicine, 1994. **5**(6-7): p. 314-319.

25. Daniel, M., *Contact stresses in the human hip joint - review.* Bulletin of Allpied Mechanics, 2006. **2**(8): p. 197-203.

26. Skripitz, R., Aspenberg, P., *Tensile bond between bone and titanium - a reappraisal of osseintegration.* Acta Orthopaedica Scandinavica, 1998. **69**(3): p. 315-319.

27. Joshi, M.G., Advani, S.G., Miller, F., Santare, M.H., *Analysis of a femoral hip prosthesis designed to reduce stress shielding.* Journal of Biomechanics, 2000. **33**(12): p. 1655-1662.

28. Tarala, M., Waanders, D., Biemond, J.E., Hannink, G., Janssen, D., Buma, P., and Verdonschot, N, *The effect of bone ingrowth depth on the tensile and shear strength of the implant–bone e-beam produced interface.* Journal of Materials Science-Materials in Medicine, 2011. **22**(10): p. 2339-2346.

29. Li, X., Wang, C.T., Zhang, W.G., Li, Y.C., *Fabrication and characterization of porous Ti6Al4V parts for biomedical applications using electron beam melting process.* Materials Letters, 2009. **63**(3-4): p. 403-405.

30. Akahori, T., Niinomi, M., Fukui, H., Ogawa, M., Toda, H., *Improvement in fatigue characteristics of newly developed beta type titanium alloy for biomedical applications by thermo-mechanical treatments.* Materials Science & Engineering C-Biomimetic and Supramolecular Systems, 2005. **25**(3): p. 248-254.

31. Cui, W.F., Guo, A.H., *Microstructures and properties of biomedical TiNbZrFe Beta-titanium alloy under aging conditions.* Materials Science & Engineering A, 2009. **527**: p. 258-262.

32. Niinomi, M., *Mechanical properties of biomedical titanium alloys.* Materials Science and Engineering a-Structural Materials Properties Microstructure and Processing, 1998. **243**(1-2): p. 231-236.

33. Takahashi, M., Kobayashi, E., Doi, H., Yoneyama, T., Hamanaka, H., *Phase stability and mechanical properties of biomedical beta type titanium-zirconium based alloys containing niobium.* Journal of the Japan Institute of Metals, 2000. **64**(11): p. 1120-1126.

34. Zhou, Y., Luo, D., *Microstructures and mechanical properties of Ti-Mo alloys cold-rolled and heat-treated.* Materials Characterization, 2011. **62**(10): p. 931-937.

35. Schmalzried, T.P., Jasty, M., and Harris, W.H., *Periprosthetic Bone Loss in Total Hip Arthroplasty.* The Journal of Bone and Joint Surgery, 1992. **74-A**(6): p. 849-863.

36. De Jong, P.T., Tigchelaar, W., Van Noorden, C.J.F., and Van der Vis, H.M., *Polyethylene wear particles do not induce inflammation or gelatinase (MMP-2 and MMP-9) activity in fibrous tissue interfaces of loosening total hip arthroplasties.* Acta Histochemica, 2011. **113**(5): p. 556-563.

37. Chanalit, C., Fitzsimmons, J.S., Shukla, D.R., An, K.N., O'Driscoll, S.W., *Micromotion of plasma spray versus grit-blasted radial head prosthetic stem surface.* Journal of Shoulder and Elbow Surgery, 2011. **20**(5): p. 717-722.

38. Yamamoto, O., Alvarez, K., Kikuchi, T., Fukuda, M., *Fabrication and characterization of oxygen-diffused titanium for biomedical applications.* Acta Biomaterialia, 2009. **5**: p. 3605-3615.

39. Nakai, M., Niinomi, M., Akahori, T., Yamanoi, H., Itsuno, S., Haraguchi, N., Itoh, Y., Ogasawara, T., Onishi, T., Shindoh, T., *Effect of Silane Coupling Treatment on Mechanical Properties of Porous Pure Titanium Filled with PMMA for Biomedical Applications.* Journal of the Japan Institute of Metals, 2008. **72**(10): p. 839-845.

40. Patel, M., Fisher, J. P., *Biomaterial scaffolds in pediatric tissue engineering.* Pediatric Research, 2008. **63**(5): p. 497-501.

41. Akahori, T., Niinomi, M., Nakai, M., Kasuga, T., Ogawa, M., *Characteristics of biomedical beta-type titanium alloy subjected to coating.* Materials Transactions, 2008. **49**(2): p. 365-371.

42. Buchanan, J.M., *17 year review of hydroxyapatite ceramic coated hip implants - A clinical and histological evaluation.* Bioceramics 18, Pts 1 and 2, 2006. **309-311**: p. 1341-1344.

43. Hermida, J., Yang, X.F., Li, P.J., Patil, S., Colwell, C.W., D'Lima, D.D., *Increased bone ingrowth on a biomimetic nanocrystalline apatite surface.* Bioceramics 17, 2005. **17**: p. 175-178.

44. Piscanec, S., Ciacchi, L.C., Vesselli, E., Comelli, G., Sbaizero, O., Meriani, S., De Vita, A., *Bioactivity of TiN-coated titanium implants.* Acta Materialia, 2004. **52**(5): p. 1237-1245.

45. Yang, C.Y., Chen, C.R., Chang, E., Lee, T.M., *Characteristics of hydroxyapatite coated titanium porous coatings on Ti-6Al-4V substrates by plasma sprayed*

method. Journal of Biomedical Materials Research Part B-Applied Biomaterials, 2007. **82B**(2): p. 450-459.

46.   Wazen, R.M., Lefebvre, L.P., Baril E., and Nanci A., *Initial evaluation of bone ingrowth into a novel porous titanium coating.* Journal of Biomedical Materials Research Part B, Applied Biomaterials, 2010. **94**(1): p. 64-71.

47.   Spoerke, E.D., Murray, N.G., Li, H.L., Brinson, L.C., Dunand, D.C., Stupp, S.I., *Titanium with aligned, elongated pores for orthopedic tissue engineering applications.* Journal of Biomedical Materials Research Part A, 2008. **84A**(2): p. 402-412.

48.   Chen, L., Li, T., He, H., Hu, Y., *Porous titanium implants fabricated by metal injection molding.* Trans. Nonferrous Metals Soc. China, 2009. **19**: p. 1174-1179.

49.   Hermida, J.C., Patil, S., Dimaano, F., Hawkins, M., Colwell, C.W., D'Lima, D.D., *Solution deposition of hydroxyapatite on a highly porous titanium surface enhances osseointegration.* Bioceramics 17, 2005. **17**: p. 215-218.

50.   Laptev, A., Bram, M., Buchkremer, H.P., Stover, D., *Study of production route for titanium parts combining very high porosity and complex shape.* Powder Metallurgy, 2004. **47**(1): p. 85-92.

51.   Parthasarathy, J., Starly, B., Raman, S., Christensen, A., *Mechanical evaluation of porous titanium (Ti6Al4V) structures with Electron Beam Melting.* Journal of the Mechanical Behavior of Biomedical Materials, 2009. **3**(3).

52.   Shen, H., Li, H., Brinson, L.C., *Effect of microstructural configurations on the mechanical responses of porous titanium: A numerical design of experiment analysis for orthopedic applications.* Mechanics of Materials, 2008. **40**(9): p. 708-720.

53.   Gauthier, O., Bouler, J.M., Aguado, E., Pilet, P., Daculsi, G., *Macroporous biphasic calcium phosphate ceramics: influence of macropore diameter and macroporosity percentage on bone ingrowth.* Biomaterials, 1998. **19**(1-3): p. 133-139.

54.   Hulbert, S.F., Morrison, S.J., Klawitte.J.J., *Tissue Reaction to 3 Ceramics of Porous and Non-Porous Structures.* Journal of Biomedical Materials Research, 1972. **6**(5): p. 347-374.

55.   Kong, L., Ao, Q., Wang, A., Gong, K., Wang, X., Lu, G.Y., Gong, Y.D., Zhao, N.M., Zhang, X.F., *Preparation and characterization of a multilayer biomimetic scaffold for bone tissue engineering.* Journal of Biomaterials Applications, 2007. **22**(3): p. 223-239.

56.   Lu, J.X., Flautre, B., Anselme, K., Hardouin, P., Gallur, A., Descamps, M., Thierry, B., *Role of interconnections in porous bioceramics on bone*

recolonization in vitro and in vivo. Journal of Materials Science-Materials in Medicine, 1999. **10**(2): p. 111-120.

57.   White, E., Shors, E.C., *Biomaterial Aspects of Interpore-200 Porous Hydroxyapatite.* Dental Clinics of North America, 1986. **30**(1): p. 49-67.

58.   Heinl, P., Müller, L., Körner, C., Singer, R.F., Müller, F.A., *Cellular Ti–6Al–4V structures with interconnected macro porosity for bone implants fabricated by selective electron beam melting.* Acta Biomaterialia, 2008. **4**(5): p. 1536-1544.

59.   Fukuda, A., Takemoto, M., Saito, T., Fujibayashi, S., Neo, M., Pattanayak, D.K., Matsushita, T., Sasaki, K., Nishida, N., Nakamura, T., *Osteoinduction of porous Ti implants with a channel structure fabricated by selective laser melting.* Acta Biomaterialia, 2011. **7**(5): p. 2327-2336.

60.   Bernard, S., Balla, V.M., Bose, S., Bandyopadhyay, A., *Rotating bending fatigue response of laser processed porous NiTi alloy.* Materials Science and Engineering: C, 2010. **31**(4): p. 815-820.

61.   Harcuba, P., Bacakova, L., Strasky, J., Bacakova, M., Novotna, K., Janacek, M., *Surface treatment by electric discharge machining of Ti-6Al-4V alloy for potential application in orthopaedics.* Journal of the Mechanical Behavior of Biomedical Materials, 2011. **7**: p. 96-105.

62.   Zhang, H., Zhao, C., Fan, H., Zhang, H., Pei, F., Wang, G., *Histological and biomechanical study of repairing rabbit radius segmental bone defect with porous titanium.* Journal of Peking University, Health Sciences, 2011. **43**(5): p. 724-729.

63.   Jebahi, S., Saoudi, M., Badreaoui, R., Rebai, T., Oudadesse, H., Ellouz, Z., Keskese, H., El Feki, A., El Feki, H., *Biologic response to carbonated hydroxyapatite assosiated with orthopedic device: experimental study in a rabbit model.* The Korean Journal of Pathology, 2012. **46**: p. 48-54.

64.   *ANSYS Manual-Engineering Analysis System, Ed. 10.0.* 2005, Swanson Analysis Systems (SAS) Inc.

65.   Turner, C.H., Wang, R., Burr, D.B., *Shear strength and fatigue properties of human cortical bone determined from pure sheat tests.* Calcified Tissue International, 2001. **69**(6): p. 373-378.

Paul Lambert

10364 Old Frederick Road, Woodstock, MD, 21163
410-979-7588   paulklambert@gmail.com

Education

M.S. in Materials Science and Engineering (2012):
>University of Maryland, College Park
>>GPA: 3.67/4.0

B.S. in Materials Science and Engineering (2010):
>University of Maryland, College Park
>>GPA: 3.86/4.0 (Cum Laude)
>>University Honors Program Citation
>>Minor in Music Performance

Experience

2010 Autumn-2012 Spring:
>Undergraduate/Graduate Researcher (Prof. Ankem, UMCP department of MSE)
>>Collaborated on the creation of educational teaching modules on corrosion in nuclear power plants for use by the Nuclear Regulatory Commission.

2009 Summer, 2010 Summer, 2011 Summer:
>NREIP Intern (Naval Surface Warfare Center, Carderock division)
>>Conducted fundamental research and process optimization experiments on magnetostrictive iron alloys for naval and industrial applications.

2008 Autumn:
>Volunteer Lab Assistant (Prof. Oehrlein, UMD department of MSE)
>>Facilitated research by organizing and interpreting data on plasma etch rates of silicon and various photoresists.

2007-2008:
>Lab Assistant (Prof. Greene, UMCP department of Physics)
>>Synthesized and characterized superconducting oxide films with the aim of reducing residual resistivity in the films by varying synthesis parameters.

Honors

- Dept.of Materials Science and Engineering Outstanding Senior Award Recipient, 2011
- Alpha Sigma Mu Honor Society Member, 2011-present
- ASM International Morgan L. Williams Scholarship Recipient, 2010
- Tau Beta Pi Honor Society Member, 2009-present
- Banneker/Key Scholarship Recipient, 2006-2010
- Bardasis Research Scholarship Recipient, 2007

Publications

- G. Petculescu, P.K. Lambert, A.E. Clark, K.B. Hathaway, Q. Xing, T.A. Lograsso, J.B. Restorff and M. Wun-Fogle, "Temperature dependence of magnetoelastic properties of $Fe_{100-x}Si_x$ (5<x<20), *Journal of Applied Physics*, Vol. 111, 07A921 (20120), http://dx.doi.org/10.1063/1.3673857